

## ON THE NATURE OF FOSSIL GALAXY GROUPS: ARE THEY REALLY FOSSILS ?

LA BARBERA, F.<sup>1</sup>, DE CARVALHO, R.R.<sup>2,3</sup>, DE LA ROSA, I.G.<sup>4</sup>, SORRENTINO, G.<sup>1</sup>, GAL, R.R.<sup>5</sup>, KOHL-MOREIRA, J.L.<sup>6</sup>

*Draft version August 31, 2021*

### ABSTRACT

We use SDSS-DR4 photometric and spectroscopic data out to redshift  $z \sim 0.1$  combined with ROSAT All Sky Survey X-ray data to produce a sample of twenty-five fossil groups (FGs), defined as bound systems dominated by a single, luminous elliptical galaxy with extended X-ray emission. We examine possible biases introduced by varying the parameters used to define the sample and the main pitfalls are discussed. The spatial density of FGs, estimated via the  $V/V_{\text{MAX}}$  test, is  $2.83 \times 10^{-6} h_{75}^3 \text{ Mpc}^{-3}$  for  $L_X > 0.89 \times 10^{42} h_{75}^{-2} \text{ erg s}^{-1}$  consistent with Vikhlinin et al. (1999), who examined an X-ray overluminous elliptical galaxy sample (OLEG). We compare the general properties of FGs identified here with a sample of bright field ellipticals generated from the same dataset. These two samples show no differences in the distribution of neighboring faint galaxy density excess, distance from the red sequence in the color-magnitude diagram, and structural parameters such as  $a_4$  and internal color gradients. Furthermore, examination of stellar populations shows that our twenty-five FGs have similar ages, metallicities, and  $\alpha$ -enhancement as the bright field ellipticals, undermining the idea that these systems represent fossils of a physical mechanism that occurred at high redshift. Our study reveals no difference between FGs and field ellipticals, suggesting that FGs might not be a distinct family of true fossils, but rather the final stage of mass assembly in the Universe.

*Subject headings:* Galaxies: formation – Galaxies: evolution – Galaxies: fundamental parameters

### 1. INTRODUCTION

Searching for preserved remnants of physical processes that occurred in the cosmic past is one of cosmologists' main tools in developing our understanding of how galaxies, groups, and clusters were formed and evolved, and ultimately came to define the large scale structure we observe. Recent studies have shown that there seems to be a class of systems with exceptional preservation, known as fossil groups (FGs, Ponman et al. 1994). These systems consist of isolated, luminous early-type galaxies embedded in an extended X-ray halo. The main motivation for seeking such galactic systems stems from the fact that the merger time scales for  $L > L^*$  group galaxies is much shorter than the cooling time scales for the hot gas component within which these bright galaxies are embedded (e.g. Barnes 1989, Ponman & Bertram 1993). In this simplistic view FGs are a natural consequence of the merging process in normal groups and therefore can be used to trace the history of coalescence in the not-so-high-redshift Universe.

From the observational viewpoint, FGs are seen in the optical as large elliptical galaxies, but with X-ray luminosities comparable to those of an entire group of galaxies ( $L_X > 4.4 \times 10^{42} \text{ ergs/s}$ ; see Jones et al. 2003, hereafter JO03). To date, no clear picture of their origin has emerged from the collected data. Two main scenarios have been suggested: FGs result from the complete

merging of galaxies that constituted a loose group in the past, collapsing at an early epoch, but never becoming incorporated into clusters (Hausman & Ostriker 1978; Ponman et al. 1994; Jones et al. 2000; Khosroshahi, Jones & Ponman 2004); or they originate from a region that inhibits formation of  $L^*$  galaxies in these groups leading to an atypical galaxy luminosity function (LF, Mulchaey & Zabludoff 1999).

These systems have been detected out to redshifts of at least  $z \sim 0.6$  (Ulmer et al. 2005), have high  $M/L$  ratios suggesting low star formation efficiency (Vikhlinin et al. 1999) and represent 8% to 20% of all systems with similar X-ray luminosities. Ten FGs are already known and well studied from optical and X-ray data (Mulchaey & Zabludoff 1999, Romer et al. 2000, hereafter R00, Jones et al. 2003, Khosroshahi, Jones, & Ponman 2004, Sun et al. 2004, Yoshioka et al. 2004, Ulmer et al. 2005). A recent paper by Santos et al. (2007) presents a sample of 34 FG candidates based on SDSS data. In this work, we use optical (SDSS) and X-ray (ROSAT All Sky Survey – RASS) data to define a sample of FG candidates. We select FGs following a strategy similar to Jones et al. (2003), using spectroscopic (age, metallicity,  $\alpha/\text{Fe}$  enhancement) and photometric ( $a_4$ , color gradient) parameters to further constrain what should be a FG. The main goal is to establish a link between FGs, compact groups and isolated ellipticals based on their global properties and simple expectations, if mergers are the dominant events determining the evolution of a FG.

This paper is organized as follows. Section 2 presents the galaxy catalog used to search for FGs, describing the parameters and the X-ray measurements that define the search. The actual selection of FGs is then detailed. Section 3 presents the control sample used to compare FG properties to those of "normal" ellipticals, which in principle did not result from merging. Section 4 discusses

<sup>1</sup> INAF-Osservatorio Astronomico di Capodimonte, Via Moiarillo 16, 80131 Napoli, ITALY

<sup>2</sup> VSTceN, via Moiarillo 16, 80131 Napoli, ITALY

<sup>3</sup> INPE/DAS Av. dos Astronautas 1758, São José dos Campos, SP Brazil

<sup>4</sup> Instituto de Astrofísica de Canarias, Tenerife, Spain

<sup>5</sup> Institute for Astronomy, 2680 Woodlawn Dr., Honolulu, HI 96822

<sup>6</sup> Observatório Nacional, Rua General José Cristino 77, Rio de Janeiro Brazil

the magnitude distribution of the brightest and second brightest galaxies of FGs, while in Section 5 we characterize the distribution of the faint galaxies around FGs. Since FGs are thought to be old systems, in Section 6 we examine the colors of FGs relative to the red sequence of early type galaxies. Section 7 deals with the internal structure of seed galaxies of FGs, as measured by their structural parameters and internal color gradients. In Section 8, we analyze stellar population properties of FGs, by looking at the distributions of age, metallicity, and  $\alpha$  enhancement. Finally, in Section 9, we summarize and discuss the main results. Throughout the paper we use a cosmology with  $\Omega_m = 0.3$ ,  $\Omega_\Lambda = 0.7$ , and  $H_0 = 75 \text{ km s}^{-1} \text{ Mpc}^{-1}$ .

## 2. SELECTION OF FGS

FGs are defined as bound systems of galaxies associated with extended X-ray sources. The total optical luminosity of these systems is dominated by a bright elliptical galaxy, and their LF exhibits a gap between the first and second rank galaxies (see e.g. Jones et al. 2003). The sample of FG candidates defined here is selected on the basis of spectroscopic and photometric data from the Data Release 4 (DR4) of the Sloan Digital Sky Survey (SDSS), and on the basis of RASS X-ray imaging. The optical selection is described in Sec. 2.1, while the X-ray measurements and the definition of the FG sample are presented in Sec. 2.2.

### 2.1. The SDSS catalog and the optical selection parameters

The optical selection is performed on a complete volume-limited catalog of 91563 galaxies, retrieved from the SDSS-DR4 database<sup>7</sup> through the CasJobs facility<sup>8</sup>. The catalog consists of all galaxies with absolute  $r$ -band magnitudes  $M_r$  brighter than  $-20$  and with spectroscopic redshifts between 0.05 and 0.095. Absolute magnitudes are obtained from the SDSS  $r$ -band Petrosian magnitudes, corrected for galactic extinction using the reddening maps of Schlegel, Finkbeiner and Davis (1998). The lower redshift limit of the catalog is chosen to minimize the aperture bias (Gómez et al. 2003), which strongly affects large nearby galaxies, while the upper redshift limit guarantees a high level of completeness, estimated through Schmidt's  $V/V_{max}$  test (see Sorrentino et al. 2006). The magnitude limit of  $-20$  corresponds approximately to the apparent magnitude limit of the SDSS spectroscopy at redshift  $z \sim 0.095$  ( $r \sim 17.8$ ).

Since FGs are systems characterized by a gap in the galaxy LF, we first select optical candidates by searching the SDSS spectroscopic database for pairs of galaxies whose magnitude difference is larger than a given value,  $\Delta M_{\min}$ . For each galaxy in the catalog, we select all objects whose projected distance on the sky from the target galaxy is smaller than a maximum radius,  $D_{\max}$ , and whose redshift difference is smaller than a given value,  $\Delta(cz_{\max})$ . In other words, for each galaxy, we select companion galaxies in a cylinder centered on the galaxy, with a radius of  $D_{\max}$  and a semi-height of  $\Delta(cz_{\max})$  along the line of sight. The value of  $D_{\max}$  is

fixed in physical units (Mpc), and the selection is done by transforming the value of  $D_{\max}$  to the apparent size that corresponds to the redshift of the seed galaxy. A bright galaxy is defined as a possible FG if (i) there is at least one companion selected through the above procedure, and (ii) if all the companions are fainter, with the magnitude difference greater than  $\Delta M_{\min}$ . Thus, our optical FG candidates are selected on the basis of three parameters:  $\Delta(cz_{\max})$ ,  $D_{\max}$ , and  $\Delta M_{\min}$ . The parameters  $\Delta(cz_{\max})$  and  $D_{\max}$  are used to select the companions of a given galaxy in the SDSS catalog, while the parameter  $\Delta M_{\min}$  characterizes the gap in the LF between the galaxy and its companions.

To determine suitable values of  $\Delta(cz_{\max})$ ,  $D_{\max}$  and  $\Delta M_{\min}$ , we examine how the number of optical FG candidates and the corresponding contamination rate change as a function of these parameters. The parameters are chosen in such a way that the contamination rate is at most 15%, defined as the fraction of FG candidates that would be selected (for a given set of values of  $\Delta(cz_{\max})$ ,  $D_{\max}$  and  $\Delta M_{\min}$ ) from a random distribution of galaxies with the same mean galaxy surface density, magnitude, and redshift distributions as the SDSS catalog. We generated randomized galaxy catalogs by applying the shuffling method, as described in Gal et al. (2003). First, we bin the SDSS catalog in  $4^\circ$  in right ascension and declination and  $\Delta z = 0.005$  in redshift. The randomized catalog is then obtained by shuffling galaxies in each bin by randomly exchanging their right ascension, declination and redshift. The above bin sizes are chosen such that both the mean surface density and the redshift distribution of galaxies in the SDSS catalog are preserved, without overly reducing the number of galaxies in each bin. We verified that varying these bin sizes by 20% does not change the contamination rate estimates. Fig. 1 compares the characteristics of the galaxy catalog with those of one of the shuffled catalogs. The shuffled catalogs reproduce well the sky coverage of the SDSS-DR4 catalog as well as the corresponding distributions of galaxy magnitudes and redshifts. Since the shuffling procedure washes out small scale structures from the galaxy catalog, the FG candidates that are selected from the shuffled catalogs only arise as rare and random instances in the magnitude, redshift, and spatial distributions of the galaxies, instead of a population of objects that follow from some physical evolutionary path. To reduce statistical fluctuations in the contamination rate estimates, we repeat the shuffling procedure 100 times and estimate the contamination rate as the ratio of the number of optical FG candidates to the mean number of candidates selected from the shuffled catalogs applying the same  $\Delta(cz_{\max})$ ,  $D_{\max}$ , and  $\Delta M_{\min}$  criteria.

Figs. 2 and 3 show the number of FG optical candidates and the contamination rate as functions of  $\Delta(cz_{\max})$ ,  $D_{\max}$  and  $\Delta M_{\min}$ . We vary  $\Delta(cz_{\max})$  from 0.00025 ( $\sim 75 \text{ km s}^{-1}$ ), corresponding to  $\sim 2.5$  times the typical redshift uncertainty of the SDSS spectroscopic sample<sup>9</sup>, to 0.0065, corresponding to  $\sim 2000 \text{ km s}^{-1}$ , i.e., about two times the typical velocity dispersion of a rich cluster of galaxies. The minimum value of  $D_{\max}$  is chosen to be 0.3Mpc, which is about twice

<sup>7</sup> <http://www.sdss.org/DR4>

<sup>8</sup> <http://casjobs.sdss.org/casjobs/>

<sup>9</sup> For the SDSS-DR4 main galaxy sample, the typical redshift accuracy is  $30 \text{ km s}^{-1}$  (see <http://www.sdss.org/dr4/>)

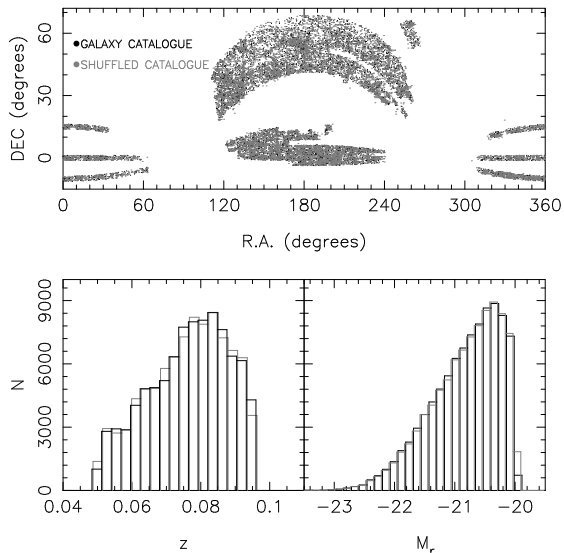


FIG. 1.— Comparison of the characteristics of the galaxy catalog with those of one of the shuffled catalogs. The upper panel plots declination versus right ascension and compares the sky area covered from both catalogs. The lower left and right panels show the redshift and magnitude distributions, respectively, of galaxies in both catalogs. As shown in the upper panel, galaxies from the shuffled and the galaxy catalogs are plotted with grey and black colors, respectively.

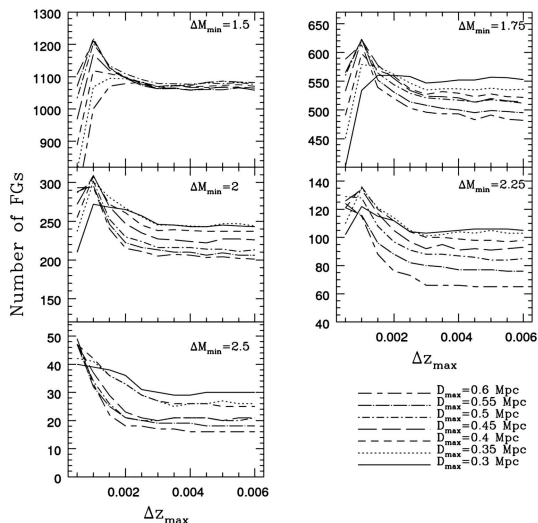


FIG. 2.— Number of FG candidates as a function of the selection parameter  $\Delta z_{\max}$ . The panels correspond to different values of  $\Delta M_{\min}$  (shown in the upper right of each plot), while different line styles correspond to different values of  $D_{\max}$ , as shown in the lower right corner of the figure.

the typical core radius of galaxy clusters (Adami et al. 1998). Furthermore, we consider only values of  $D_{\max}$  smaller than 0.6 Mpc, since higher values yield contamination rates greater than  $\sim 20\%$  for all possible values of the other two parameters. Finally, we consider only values of  $\Delta M_{\min}$  in the range of 1.5 to 2.5 mag. The value of 1.5 is chosen to have a reasonable minimum gap in the LF of FG candidates, while values of  $\Delta M_{\min}$  larger than 2.5 are excluded since they overly

reduce the number of candidates. Looking at Fig. 2, we see that the number of candidates shows a maximum at  $\Delta(cz_{\max}) \sim 0.001$  for a wide range of values of both  $D_{\max}$  and  $\Delta M_{\min}$ . Hence, to maximize the sample size, we adopt this value of  $\Delta(cz_{\max})$ . For  $D_{\max}$ , we see that for fixed values of  $\Delta(cz_{\max})$  and  $\Delta M_{\min}$  the number of candidates does not change significantly for  $0.35 \lesssim D_{\max} \lesssim 0.5$  Mpc. On the other hand, the contamination rate changes by a factor of 2 over the full range of values of  $D_{\max}$ . We choose a suitable value of  $D_{\max}$  by fixing an upper limit to the contamination rate. Examining Fig. 3 and considering all the values of  $\Delta M_{\min}$  that correspond to  $\Delta(cz_{\max}) = 0.001$ , contamination rates less than 15% are achieved only for  $D_{\max} \lesssim 0.35$  Mpc. Since the number of FG candidates decreases as a function of  $D_{\max}$ , we adopt  $D_{\max} = 0.35$  Mpc. Finally, we have to determine the choice of  $\Delta M_{\min}$ . Fig. 4 plots the contamination rate as a function of  $\Delta M_{\min}$  for all possible values of  $D_{\max}$  and  $\Delta(cz_{\max})$ . We see that the contamination is almost constant for  $\Delta M_{\min} \lesssim 2.2$ , with an increase for larger values of  $\Delta M_{\min}$ . Fig. 5 plots the number of FG candidates as a function of  $\Delta M_{\min}$  for  $\Delta(cz_{\max}) = 0.001$  and  $D_{\max} = 0.35$  Mpc. The number of FG candidates rapidly decreases as  $\Delta M_{\min}$  increases, reaching almost 0 at  $\Delta M_{\min} \sim 2.5$ . In order to obtain a statistically significant number of FG candidates without overly reducing the  $\Delta M_{\min}$  gap, we decided to adopt  $\Delta M_{\min} = 1.75$  mag.

To summarize, the values of the three parameters  $\Delta(cz_{\max})$ ,  $D_{\max}$  and  $\Delta M_{\min}$  are chosen as a compromise between the number of selected FG candidates and the corresponding contamination rates. We adopt the following parameters:  $\Delta(cz_{\max}) = 0.001$ ,  $D_{\max} = 0.35$  Mpc and  $\Delta M_{\min} = 1.75$  mag, resulting in a list of 578 optical FG candidates. Note that the  $D_{\max}$  value is close to half of the virial radius ( $0.37 h_{75}^{-1}$  Mpc) assuming a temperature of 1 Kev and the mean redshift of the sample (Evrard et al. 1996). As found by Khosroshahi et al. (2007), based on Chandra data, a typical temperature for FGs is 1 Kev, with a few systems having a temperature as high as  $\sim 3$  Kev. In the latter case, half the virial radius is 0.64 Mpc. Using such a large  $D_{\max}$  results in a high contamination rate for whatever value of  $\Delta(cz_{\max})$  and  $\Delta M_{\min}$  (see Fig. 4).

We note that the above selection of FG systems can be affected by the SDSS spectroscopic incompleteness, because of the SDSS fiber collision limit preventing neighboring fibers from being closer than  $55''$ . This prevents complete spectroscopic coverage of objects in dense regions, even in cases where multiple tiles overlap. It is therefore, possible to have galaxies adjacent to some optical FG candidates which would nominally disqualify them, but lacking SDSS spectroscopy, the neighbors would not be taken into account by our selection procedure. This issue is addressed in Sec. 2.2.2.

## 2.2. X-ray Analysis and the Final Sample of FGs

### 2.2.1. Measuring X-ray Fluxes with RASS

The X-ray luminosity  $L_X$  of each optical FG candidate is estimated using RASS countrates<sup>10</sup>. The first step is to estimate the background contribution, by randomly selecting one hundred boxes each with an area of 100

<sup>10</sup> ftp://ftp.xray.mpe.mpg.de/rosat/archive/900000

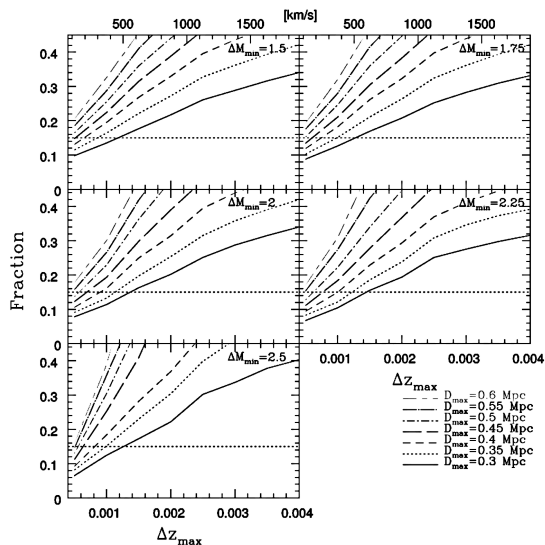


FIG. 3.— Same as Fig. 2 but showing the corresponding contamination rates as estimated through the shuffling method (see the text). In each panel, the dotted horizontal line marks the upper limit for the acceptable level of contamination in the sample of FG candidates.

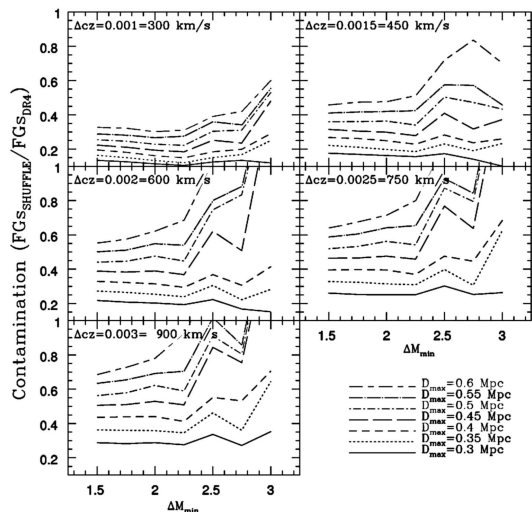


FIG. 4.— Contamination rate as a function of  $\Delta M_{\min}$ . Each plot corresponds to a different value of  $\Delta(cz_{\max})$ , as shown in the upper-right of each panel. Curves with different line styles correspond to different values of  $D_{\max}$ , and are the same as in Fig. 2.

square arcminutes, located throughout the  $6.5^\circ \times 6.5^\circ$  field containing the target, and then taking the median and rms of these hundred values. The count rates are integrated in three apertures, with radii of 5, 10, and 20 times the effective radius,  $r_e$ , of the FG seed galaxies. Effective radii are measured from the  $r$ -band SDSS images, as described in App. C. We considered a detection as significant when the S/N is at least  $3\text{-}\sigma$  above the background, otherwise we derive upper limits as in Beuing et al. (1999). We selected for further analysis only those systems with a significant X-ray detection in at least one of the three measured apertures, resulting in a sample of 113 (out of 578) FG candidates.

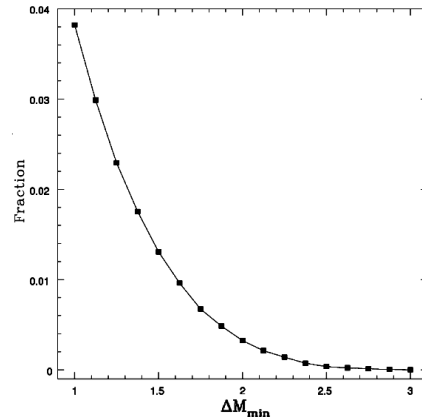


FIG. 5.— Fraction of FG candidates in the SDSS catalog as a function of  $\Delta M_{\min}$  for the values of  $D_{\max} = 0.35\text{Mpc}$  and  $\Delta(cz_{\max}) = 0.001$  adopted to select FG candidates. The black curve is obtained from a cubic interpolation of the data.

To convert the measured total count rate into an unabsorbed X-ray flux in the ROSAT 0.5 - 2.0 keV energy band, we use the HEASARC PIMMS tool. We assume a Raymond-Smith spectrum to represent the hot plasma present in the intracluster medium (Raymond & Smith 1977) with solar metallicity and an interstellar hydrogen column density along the line-of-sight given by Bajaja et al. (2005). The plasma temperature is fixed at 1 keV, which is typical for very bright elliptical galaxies (Beuing et al. 1999), although the dependence of the flux on the temperature used is insignificant ( $< 5\%$ ). Finally, the rest frame 0.5-2.0 keV flux was obtained by applying the K-correction as in Böhringer et al. (2000).

### 2.2.2. Contamination by Spirals, AGN, and Clusters

To refine the selection of FGs, we considered four possible sources of contamination: (i) spiral galaxies; (ii) AGN; (iii) superpositions with rich clusters of galaxies.

(i) Since FGs are dominated by a bright elliptical galaxy, we removed contaminating spiral galaxies from the list of optical candidates. We fit the SDSS  $r$ -band image of each galaxy with a seeing convolved Sersic model (see App. C for details), and flagged as spirals those objects with a detectable spiral arm pattern in the residual map obtained after model subtraction. This procedure eliminates ninety-one (out of 578) contaminating systems.

(ii) We flagged those FG optical candidates with AGN spectral signatures and excluded them from the analysis. AGN were selected following the criteria described in Sorrentino et al. (2006). We removed forty-five (out of 578) galaxies.

The above selections leave a sample of 102 FG candidates with significant X-ray detections, no significant AGN signatures, and early-type morphology.

(iii) The resolution and S/N of RASS is insufficient to differentiate between X-ray emission from a real FG and that from a rich cluster which happens to be along the line of sight. Moreover, for a rich cluster, the SDSS spectroscopic incompleteness at the bright end might mimic the lack of bright companion galaxies required to be a FG. Thus, we rejected FG candidates within 1.5 Mpc (at the FG redshift) from a rich Abell cluster. We discarded

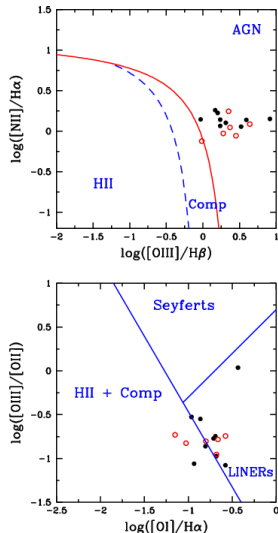


FIG. 6.— Diagnostic diagrams showing the nine FG candidates (filled circles) which still show some emission lines in the SDSS spectra. The empty circles represent the six field galaxies (FS; see Sec. 3) with some residual emission features in the SDSS spectra. We also display the regions defining the locus for AGN (Seyfert and LINERs) and starbursts (HII). Notice that the figure also shows the transition region between AGN and HII (Comp).

$R > 0$  Abell clusters with the exception of Abell 690 (richness  $R = 1$ ; FG 22 of Tab. 2) for which we verified that there are no galaxies with available photometry from SDSS that might invalidate our adopted fossilness definition. Twenty-eight (out of 102) FG candidates were discarded with this criterion, leaving a sample of seventy-four FG candidates.

Although we eliminated AGN and spiral galaxies from the sample, we further investigated the presence of elusive emission lines in the SDSS spectra of the 102 FGs with significant X-ray detections. For each spectrum, we modeled the absorption lines with a combination of stellar population models using the STARLIGHT code (Cid Fernandes et al. 2005). Further details of the procedure are presented in Sec. 8. After subtracting the old stellar component, we measured the remaining  $O_I$ ,  $O_{II}$ ,  $O_{III}$ ,  $H_\alpha$ ,  $H_\beta$ , and  $N_{II}$  emission features. Fig. 6 displays the diagnostic diagrams defined with these indices. Regions corresponding to different types of active galaxies are plotted according to the definition of Kewley et al. (2006). Only nine FG candidates have residual emission lines typical of AGN. In agreement with expectations from our morphological selection, no starburst galaxies (HII) are found in the FG sample. Moreover, almost all of the AGN are classified as LINERs, which have a typical X-ray luminosity of  $10^{40}$  ergs/s (see Komossa et al. 1999, two orders of magnitudes lower than the minimum X-ray luminosity of the FGs in our sample. Thus, we conclude that AGN and starburst contamination does not contribute significantly to the X-ray measurements, except for AGN that might be detected only in X-rays. However, as noted by Anderson et al. (2007), these account for only a minor fraction of all AGN.

### 2.2.3. How extended is the X-ray emission?

An important issue to consider is whether the observed X-ray luminosity comes from an extended source. Al-

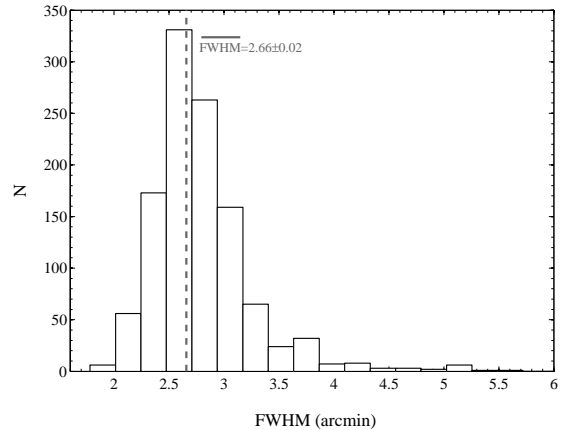


FIG. 7.— Distribution of FWHM values for 1232 point sources in the RASS Bright Source Catalog. The vertical dashed line marks the position of the peak of the distribution. The location of the peak,  $FWHM$ , and the corresponding  $1\sigma$  error are shown in the upper part of the figure.

though AGN were excised from our sample following the recipes in Sorrentino et al. (2006), some AGN might only be detected in X-ray (Tozzi et al. 2006; Anderson et al. 2007), representing a further source of contamination in the FG sample. To objectively establish the extended nature of the X-ray emission we proceed as follows:

1 - We select 1232 point sources from the RASS Bright Source Catalog (Voges et al. 1999), requiring that the sources have a high probability of being a real detection (i.e. source detection likelihood  $> 100$ ) and a source extension of zero. This data set was used to measure the mean FWHM of the RASS PSF over the whole sky. We used 2DPHOT (La Barbera et al 2008) to fit a Moffat distribution to every source, after a gaussian smoothing (with a  $\sigma$  of one pixel) of the original count rate image. The smoothing was done similarly for the FGs (see below). Fig. 7 shows the distribution of the FWHM for the 1232 point sources. The location of the peak of the distribution (and its error) was obtained from the bi-weight estimator (Beers et al. 1990) and is found to be  $2.66(\pm 0.02)$  arcmin. The narrowness of the distribution confirms the expectations that the RASS PSF has little off-axis variation resulting from the scanning strategy. We also verified that fitting the unsmoothed images gives a mean FWHM of 2.15 arcmin, in good agreement with the value of 2.1 arcmin from de Grandi et al. (1997).

2 - For the seventy-four FGs, we smoothed the original RASS images with a 1-pixel Gaussian (as for the point sources). Source detection was performed using S-Extractor with a detection threshold of  $2\sigma$  over an area of 5 pixels, using a tophat detection filter, which is optimal for faint source detection. The gaussian smoothing enhances the contrast over the background. For each FG, we identified the closest X-ray source to the SDSS position.

3 - Using the smoothed X-ray images, we fit a Moffat distribution to the FG candidates. Here, the error in the FWHM was estimated from one-hundred Monte Carlo simulations. For each simulation, all the detected sources were masked from the original RASS image and the remaining pixels were bootstrapped to create a random background image, which was then gaussian smoothed.

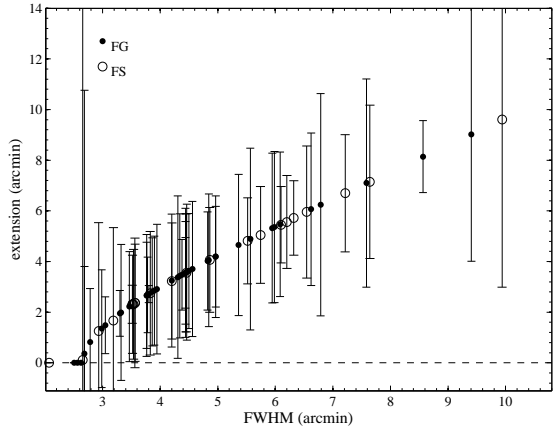


FIG. 8.— Extension parameter versus FWHM for the 43 FG candidates (filled circles) with an associated X-ray source. Empty circles represent the sample of twenty-two field galaxies defined in Sec. 3. The error bars show  $2\sigma$  standard uncertainties. Sources are defined as extended if their error bar does not cross the horizontal dashed line corresponding to a zero extension.

The Moffat model was added to this image, and the fitting was repeated. We subtracted in quadrature the mean FWHM of the RASS smoothed PSF from the FWHM of each source. This quantity was defined as the source extension, with its error computed from the uncertainty on the FWHM.

4 - We matched X-ray and optical sources by considering only cases where the distance between the optical and X-ray FG positions were smaller than the FWHM of the X-Ray source. Only forty-three (out of seventy-four) FG candidates have X-ray counterparts meeting this requirement.

5 - We classified the FG X-ray sources as extended if the extension parameter was greater than 0 at the  $2\sigma$  level (see Fig. 8). This selection removes eight point-like FG candidates, leading to a sample of thirty-five extended FGs. In the following section, we discuss the effect of SDSS spectroscopic incompleteness on this sample.

#### 2.2.4. Spectroscopic incompleteness and the final sample

The SDSS spectroscopy is incomplete in high-density regions due to limitations on fiber placement. We address this spectroscopic incompleteness issue as follows: for each of the thirty-five FG candidates, we select all galaxies with SDSS photometry fulfilling the  $D_{\max}$  criterion and with magnitude between  $m$  and  $m + 1.75$ , where  $m$  is the FG  $r$ -band Petrosian magnitude. These are the galaxies that could possibly invalidate the fossilness definition. Then, we queried the SDSS DR6 and NED for spectroscopic redshifts of these possible contaminants. We found that for nine (out of thirty-five) FG candidates, there is at least one galaxy invalidating the  $\Delta(cz_{\max})$  criterium, hence, disqualifying the system. Using photometric redshifts, we also rejected one system with three possible contaminants having concordant redshifts within  $2\sigma$ . Applying the same analysis to the eight point-like FG candidates (see previous section) leaves four such objects having no possible gap contaminants.

After this procedure, our final sample consists of

twenty-five systems<sup>11</sup>, which we use to characterize the properties of FGs. This is the largest sample of FGs available in the low redshift regime ( $z < 0.1$ ). In Fig. 9, we show the X-ray contour plots for these FGs with the optical SDSS position overlaid. As we can see, usually, the centroid of the X-ray component coincides with the optical counterpart.

#### 2.3. Archive data and external comparison

We searched the XMM, Chandra, ASCA and Einstein archives for any publicly available data, taken with any of the instruments, within a  $1.5h_{75}^{-1}$  Mpc radius of the final samples of FGs and field galaxies (defined in Sec. 3). We found data in the vicinity of only a single FG in the Chandra archive. None of the other archives contained any observations including objects in our final sample. We conclude that there are no useful archival data deeper than the RASS to systematically examine the X-ray properties of our FG and field galaxies, or exclude them from the sample as X-ray AGN.

We also looked for FGs defined in the literature that are in the same redshift interval as our sample. Not surprisingly, we found only three systems well studied in several contributions (e.g. JO03, Khosroshahi et al. 2007), although none of them have data in the SDSS. Moreover, Santos et al. (2007), defining a sample of thirty-four FGs from SDSS-DR4, find only four systems in the same redshift regime as we consider here. One of them is in our sample of FG candidates, but with an X-ray component indistinguishable from the RASS PSF. The other three systems are not in our FG sample because the absolute magnitude limit of our SDSS catalog prevents finding a second-rank galaxy for the main targets.

#### 2.4. The Space Density of FGs

The space density of the twenty-five FGs was estimated using the  $1/V_{\max}$  statistics suggested by Avni & Bahcall (1980). The sky area is that of the DR4, 4783 square degrees. Applying various X-ray luminosity limits we find different integrated space densities, which we compared to those of previous studies. Vikhlinin et al. (1999, hereafter V99) studying an overluminous elliptical galaxy (OLEG) sample found a space density of  $1.5 \times 10^{-6} h_{75}^3 \text{ Mpc}^{-3}$  for  $L_X > 0.44 \times 10^{42} h_{75}^{-2} \text{ erg/s}$  while we find  $3.4 \times 10^{-6} h_{75}^3 \text{ Mpc}^{-3}$ . For the same limiting value of  $L_X$ , Romer et al. (2000) find  $6.7 \times 10^{-6} h_{75}^3 \text{ Mpc}^{-3}$ , JO03 finds  $6.75 \times 10^{-7} h_{75}^3 \text{ Mpc}^{-3}$ , and Dariush et al. (2007) predicts  $5.4 \times 10^{-6} h_{75}^3 \text{ Mpc}^{-3}$  based on the Millennium simulation. Considering the errors in these measurements, as presented in Table 1 of JO03, we can conclude that all these values are consistent. When a brighter limiting  $L_X$  is considered,  $L_X > 0.89 \times 10^{42} h_{75}^{-2} \text{ erg/s}$ , V99 finds  $8.1 \times 10^{-6} h_{75}^3 \text{ Mpc}^{-3}$  and we find  $2.83 \times 10^{-6} h_{75}^3 \text{ Mpc}^{-3}$ , still consistent. We emphasize that the samples analyzed by R00, V99, and JO03 have only 3, 4, and 5 systems, respectively, while we have twenty-five new FGs, yet the space densities are still very consistent.

<sup>11</sup> We note that almost all FGs in our sample have a total X-ray luminosity above the (bolometric) limit of  $4.4 \times 10^{42} \text{ erg/s}$  adopted by Jones et al. (2003). Only two FGs (FG 11 and FG 21, see Tab. 2) have an X-ray luminosity of  $\sim 2 \times 10^{42} \text{ erg/s}$ , corresponding to a bolometric value of  $\sim 3.5 \times 10^{42} \text{ erg/s}$ .

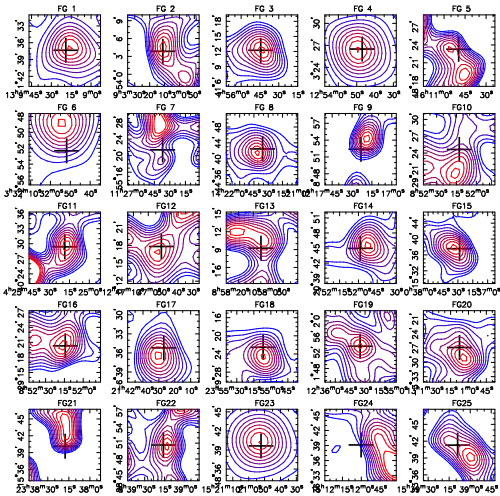


FIG. 9.— X-ray emission contours from the RASS for the twenty-five FGs, with the position of the optical SDSS galaxy image marked by a black cross. The contours have been obtained by applying a 2 pixel gaussian smoothing to the original RASS images and are equally spaced at intervals of  $1\sigma$  starting at  $0.5\sigma$  above the background. The reddest contours mark the centroid of the X-ray emission. Each panel is three times as wide as the FWHM of the X-ray source.

### 3. COMPARING THE PROPERTIES OF FGS AND FIELD GALAXIES

To establish a benchmark for the properties of FGs, we generated a control sample of galaxies with the same luminosity distribution and the same optical and X-ray properties as the FG sample. The control sample represents an idealization of a sample of systems which were probably formed by a single collapse of a protogalaxy and did not experienced any major mergers in last 3–4 Gyrs. From now on, we refer to the control sample as ‘field’ galaxies. This was created by first excluding the brightest galaxies of the FG optical candidates and their companions (see Sec. 2.1) from the whole galaxy catalog, yielding a reduced catalog with 90259 targets. We binned the sample of 578 FG optical candidates and the reduced galaxy catalog by  $r$ -band absolute magnitude, and for each bin computed the ratio between the number  $N_1$  of FG optical candidates in that bin to the number  $N_2$  of galaxies in the reduced catalog. Galaxy absolute magnitudes were computed as described in App. B. To obtain a sample of ‘field’ galaxies with the same LF as that of the seed galaxies of the 578 optical FG candidates, we randomly extracted galaxies from the reduced catalog in each magnitude bin according to the corresponding value of the ratio  $f = N_1/N_2$ . Because we have excluded the brightest galaxies and their companion galaxies in the optical FG candidates from the entire galaxy catalog, it is possible for  $N_2$  to be lower than  $N_1$ , yielding an ill-defined value of  $f$ . This is shown in Fig. 10, where we compare the LF of the brightest galaxies in the optical FG candidates with that of galaxies in the reduced catalog. At magnitudes brighter than  $M_r \sim -23$ , the number of optical FG candidates in each magnitude bin is slightly larger than the number of galaxies in the reduced catalog. To ensure that the value of  $f$  is always less than one, we enlarged the size of the brightest magnitude bins such that the condition  $N_2 < N_1$  was always fulfilled. This goal was achieved by considering the same

magnitudes bins as in Fig. 10 for  $M_r \gtrsim -22.8$ , and just one bin at brighter magnitudes, from  $M_r = -23.6$  to  $M_r \sim -22.8$ . The list of field galaxies was extracted according to this binning procedure, and, by construction, it has the same sample size ( $N = 578$ ) as the optical FG candidates. Fig. 10, which also plots the LF of this field sample, shows that its LF actually matches the LF of the seed galaxies in the optical FG candidates. As expected from the fact that we use a single, larger magnitude bin at  $M_r \lesssim -23$ , there is only a small difference between the two LFs in this magnitude range. However, this difference is only marginally significant, provided that uncertainties on number counts are taken into account.

To perform a detailed comparison between FGs and field galaxies, we extracted a subsample of field galaxies, following the same procedure adopted to select the sample of FGs from the initial list of 578 optical FG candidates (see Sec. 2.2). We removed spirals and AGN from the catalog of field galaxies, and analyzed the X-ray images of the remaining systems. Sixty-six (out of 578) field galaxies have significant X-ray detections. From these, following the prescriptions outlined in the previous section, we kept only the twenty-two galaxies associated with an X-ray source and with a projected distance from rich Abell clusters larger than 1.5Mpc. Applying the X-ray extent requirement leaves a final sample of seventeen field galaxies, shown in Fig. 8. A similar analysis to that performed in Sec. 2.2.2 for FGs shows that contamination from elusive AGN and starbursts is also negligible for the sample of field galaxies (see Fig. 6). Although selected in the same way from an optical catalog with the same number of galaxies (578) and the same galaxy LF as the FGs, the number of galaxies in the field sample with significant X-ray detections ( $N = 66$ ) is 65% less than the corresponding FG sample ( $N = 102$ ). The final FG and field samples have a similar ratio of 68%.

In the following sections, we compare the distributions of several properties (luminosity, structural parameters, internal color gradients, stellar populations) of FG and field galaxies. For each quantity, the comparison is performed (i) by a Kolmogorov-Smirnov (hereafter KS) test and (ii) by deriving the mean and width of each distribution. The mean and width values obtained for each quantity and the results of the KS tests are reported in Tab. 1. In order to reduce the effects of outliers in each distribution, the corresponding mean, and width values were computed using a  $2.5\sigma$  clipping method. We also verified that computing the location and width values with ROSTAT (Beers et al. 1990) does not affect our results. All quantities used in this analysis are reported in Tab. 2 for each FG and field galaxy (see App. A). Although not used in the present analysis, the table also lists the properties of the four FGs with point-like X-ray emission that survived the final section step described in Sec. 2.2.4. The distributions of photometric and X-ray properties of FGs and field galaxies (hereafter also referred as the field sample, FS) are presented in Fig. 11 and described in the following sections.

### 4. LUMINOSITIES OF FIRST AND SECOND RANK GALAXIES

In this section, we analyze the properties of FGs by examining the magnitude distributions of their seed and second rank galaxies as well as their X-ray fluxes.

TABLE 1  
 MEAN AND WIDTH VALUES OF THE DISTRIBUTIONS OF SEVERAL QUANTITIES FOR FG AND FS GALAXIES. THE P-VALUES FROM THE KS TEST COMPARING THE DISTRIBUTIONS OF FG AND FS PROPERTIES ARE REPORTED IN COL.(6). VALUES SMALLER THAN 0.1 INDICATE THAT THE TWO SAMPLES LIKELY DO NOT DERIVE FROM THE SAME PARENT DISTRIBUTION.

(1)	<i>FG</i>		<i>FS</i>		KS (6)
	mean (2)	width (3)	mean (4)	width (5)	
$^{0.1}M_r$	$-22.64 \pm 0.09$	$0.37 \pm 0.07$	$-22.45 \pm 0.09$	$0.37 \pm 0.05$	0.36
$\delta_N$	$2.5 \pm 0.4$	$1.56 \pm 0.30$	$2.5 \pm 0.5$	$2.0 \pm 0.4$	0.99
$\log R_e$ (kpc)	$1.13 \pm 0.08$	$0.29 \pm 0.06$	$0.97 \pm 0.08$	$0.35 \pm 0.10$	0.23
$n$	$5.4 \pm 0.6$	$2.4 \pm 0.6$	$5.5 \pm 0.6$	$2.5 \pm 0.4$	0.83
$a_4 * 100$	$0.11 \pm 0.26$	$0.6 \pm 0.3$	$0.3 \pm 0.2$	$0.75 \pm 0.11$	1.00
$\nabla(g-r)$	$-0.072 \pm 0.026$	$0.09 \pm 0.06$	$-0.17 \pm 0.08$	$0.25 \pm 0.08$	0.74
$\log L_X$ ( $\cdot 10^{44} h_{75}^{-2}$ ergs/s)	$-0.90 \pm 0.09$	$0.41 \pm 0.13$	$-0.84 \pm 0.15$	$0.52 \pm 0.11$	0.44
$\delta_{CM}$	$0.0 \pm 0.3$	$0.8 \pm 0.4$	$-0.5 \pm 0.3$	$1.1 \pm 0.2$	0.29
$\log \sigma_0$ (km/s)	$2.43 \pm 0.01$	$0.07 \pm 0.01$	$2.42 \pm 0.04$	$0.09 \pm 0.05$	0.40
$\log \text{Age}$ (Gyr)	$0.72 \pm 0.03$	$0.14 \pm 0.03$	$0.77 \pm 0.04$	$0.16 \pm 0.04$	0.10
$[Z/H]$	$0.44 \pm 0.03$	$0.17 \pm 0.02$	$0.34 \pm 0.06$	$0.24 \pm 0.05$	0.29
$[\alpha/Fe]$	$0.27 \pm 0.02$	$0.10 \pm 0.01$	$0.28 \pm 0.03$	$0.12 \pm 0.02$	0.93

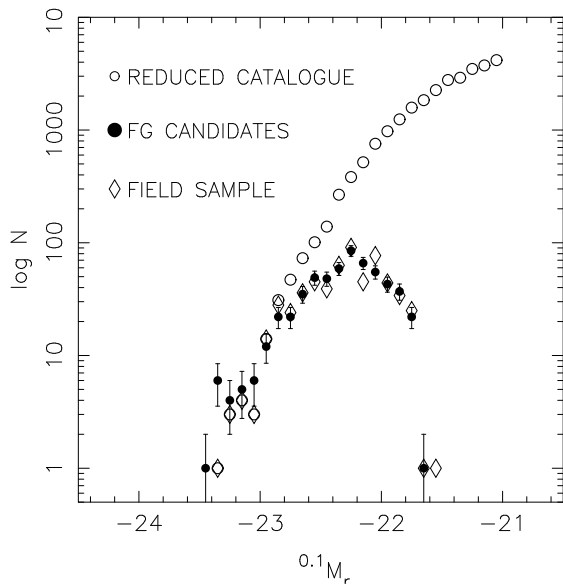


FIG. 10.— LFs of galaxies in the reduced catalog (empty circles), brightest galaxies in FG candidates (filled circles) and of galaxies in the field sample (diamonds). The symbols used for each sample are shown in the upper left part of the figure. The error bars mark  $1\sigma$  Poissonian uncertainties on number counts of FG brightest galaxies.

Fig. 11a compares the optical luminosity distributions of FG first rank galaxies with those of the corresponding field sample. The mean and width values of each distribution are reported in Tab. 1. Both the figure and the table show that the  $r$ -band LFs of FG and field galaxies are indistinguishable. This result is also confirmed by the KS test (see Tab. 1), whose p-value is  $\gtrsim 0.3$ . Fig. 11b shows that not only the optical but also the X-ray luminosities of FG galaxies are consistent with those of field galaxies. This is also clear from the mean, width, and KS test results reported in Tab.1. The fact that FG and field galaxies have the same X-ray luminosities is of particular interest, since it implies that both samples consist of galaxies embedded within halos of the same mass. Hence, any difference between FG and field samples is not related to the selection of these samples, but

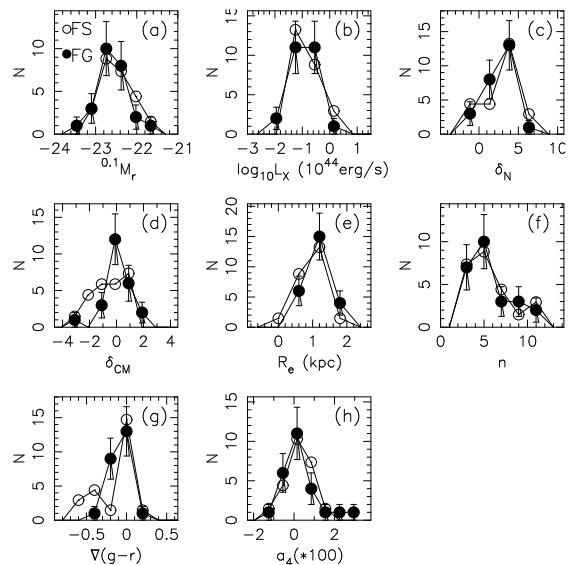


FIG. 11.— Distributions of FG and FS properties as follows: (a) absolute magnitude, (b) X-ray luminosity, (c) density excess, (d) normalized distance to the red sequence, (e)  $r$ -band effective radius, (f)  $r$ -band Sersic index, (g) internal color gradient, (h) boxiness parameter. FG and field galaxies are plotted as filled and empty circles, respectively (see upper-left panel). Error bars mark the  $1\sigma$  standard confidence intervals of FG number counts. To make the plot more readable, uncertainties on field galaxy number counts are not shown. The distribution of field galaxies is normalized to the total number of corresponding FG galaxies.

is more deeply related either to the initial conditions of the galaxy LF within the halos, or to the different evolutionary history of galaxies within the halo.

To analyze the luminosity distribution of second rank galaxies, we have to consider that the SDSS-DR4 galaxy catalog is magnitude limited and that FG optical candidates are selected as systems where the magnitude difference between the two brightest galaxies is greater than  $\Delta M_{\min}$ . This implies that a larger fraction of FGs can be selected at the brightest magnitudes of the galaxy LF. In other words, the seed galaxies of FGs do not form a magnitude complete sample. Such incompleteness is illustrated in Fig. 12, where we plot the magnitude difference  $\Delta M$  between the second and first rank galaxies



of FGs as a function of the  $r$ -band absolute magnitude,  $^{0.1}M_r$ , of the first rank galaxy. Absolute magnitudes are obtained as described in App. B, by k-correcting the Petrosian  $r$ -band magnitudes of the DR4 dataset to redshift  $z = 0.1$ . Since the SDSS galaxy catalog is limited to  $M_r = -20$ , and since, by definition, we have  $\Delta M > \Delta M_{\min} = 1.75\text{mag}$ , the seed galaxies of FGs have to fulfill the equation

$$^{0.1}M_r + ^{0.1}k_r < -20 - \Delta M \sim -21.75\text{mag}. \quad (1)$$

The term  $^{0.1}k_r$  denotes the k-correction computed as described in App. B, and is introduced in the previous equation to account for the fact that k-corrections were not applied in the computation of the  $r$ -band absolute magnitudes used to select the SDSS-DR4 catalog. Since the typical value of  $k_r$  is  $-0.13\text{mag}$ , Eq. 1 implies the constraint  $^{0.1}M_r \lesssim -21.62$ , and in fact, as shown in Fig. 12, we do not find any first rank galaxy fainter than this magnitude limit. Moreover, for a given value of  $^{0.1}M_r$ , we can only select FGs with  $^{0.1}M_r + ^{0.1}k_r + \Delta M < -20$ , which implies  $\Delta M < -^{0.1}M_r - 20 - ^{0.1}k_r \sim -^{0.1}M_r - 19.87$ . This last constraint is shown by the line in Fig. 12, and results in a larger range of allowed values of  $\Delta M$  at bright galaxy magnitudes. In other words, the selection procedure affects the magnitude distribution of FGs, biasing the sample towards a larger allowed fraction of systems at brighter magnitudes. Despite this bias, Fig. 12 shows that the brightest first rank galaxies do not show a larger range of  $\Delta M$  values, although they are allowed. At bright magnitudes, we see that seed galaxies of FGs are characterized by a larger magnitude gap. However, one has to note that the SDSS spectroscopic incompleteness due to fiber collisions might cause an overestimate of  $\Delta M$ , and that the SDSS spectroscopic survey did not target many very bright galaxies ( $r < 15.5$ ), which might reduce the number of detected FG systems at the bright end.

To better understand the distribution of  $\Delta M$  with respect to the magnitude of the seed galaxies, we ran Monte-Carlo simulations. For each seed galaxy of the 102 FG candidates, we assigned a fictitious second rank galaxy from the SDSS catalog by randomly extracting a galaxy with  $\Delta M \geq \Delta M_{\min}$ . We repeated this procedure several times ( $N = 10000$ ), and estimated the mean value of  $\Delta M$  obtained for the randomized second rank galaxies. Fig. 12 shows that this mean  $\Delta M$  value actually decreases as  $^{0.1}M_r$  increases. At magnitudes fainter than  $^{0.1}M_r \sim -23$ , the simulated  $\Delta M$  value is fully consistent with the  $\Delta M$  distribution of FGs, implying that the  $\Delta M$  vs.  $^{0.1}M_r$  correlation can be simply explained by the shape of the LF of second rank galaxies. However, at bright magnitudes ( $^{0.1}M_r < -23$ ), all the seed galaxies of FGs have  $\Delta M$  values larger than the simulations, which might reflect some intrinsic physical property of FG systems (see Sec. 9).

## 5. FAINTEST GALAXIES: DENSITY EXCESS

We characterize the population of the faintest galaxies around each FG by measuring the density excess of these galaxies with respect to the field population. Since galaxies around FGs can be fainter than the magnitude limit of the SDSS spectroscopic catalog, we measure the density excess by taking advantage of the SDSS-DR4 pho-

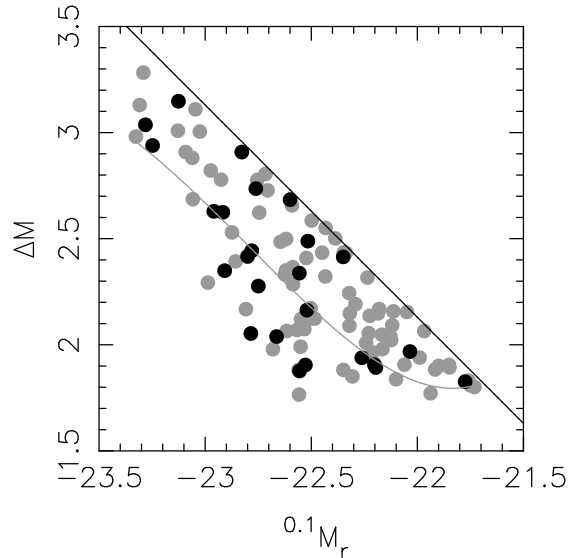


FIG. 12.— Differences between  $r$ -band magnitudes of second and first rank galaxies of FGs,  $\Delta M$ , are plotted as a function of the absolute magnitude,  $^{0.1}M_r$ , of the first rank galaxies. Grey circles denote the sample of 102 FG candidates with X-ray significant detection (see Sec. 2.2), while black symbols correspond to the final sample of twenty-five FGs. The black line marks the range of allowed values of  $\Delta M$  as a function of  $^{0.1}M_r$ , while the grey curve shows the mean  $\Delta M$  value as a function of  $^{0.1}M_r$ , obtained by randomly extracting second rank galaxies from the SDSS catalog (see the text).

tometric data, whose completeness limit<sup>12</sup> is  $\sim 22.2\text{mag}$  in  $r$ -band (Stoughton et al. 2002). The density excess,  $\delta_N$ , is defined as follows:

$$\delta_N = \frac{\rho_{\text{in}} - \rho_{\text{out}}}{\sqrt{\sigma_{\text{in}}^2 + \sigma_{\text{out}}^2}}, \quad (2)$$

where  $\rho_{\text{in}}$  is the mean galaxy density within an inner circle of radius  $r_{\text{in}}$  centered on the FG seed galaxy and  $\rho_{\text{out}}$  is the mean galaxy density in a concentric annulus with inner and outer radii of  $r_1$  and  $r_2$ , respectively. The quantities  $\sigma_{\text{in}}$  and  $\sigma_{\text{out}}$  denote the  $1\sigma$  uncertainties on  $\rho_{\text{in}}$  and  $\rho_{\text{out}}$ , which are estimated by accounting for Poisson noise in the galaxy counts. For each FG, we measure  $\delta_N$  by setting  $r_{\text{in}} = 0.25R_{\text{Abell}}$ ,  $r_1 = 1R_{\text{Abell}}$  and  $r_2 = 2R_{\text{Abell}}$ , respectively, where  $R_{\text{Abell}}$  is the apparent size corresponding to one Abell radius (1.5Mpc) at the redshift of the FG seed galaxy. We have verified that our results do not change when these radii are varied by as much as 20%. To probe a fixed range of the galaxy LF, we measure  $\rho_{\text{in}}$  and  $\rho_{\text{out}}$  using only galaxies in the magnitude range of  $m_2$  to  $m_2 + 2$ , where  $m_2$  is the magnitude of the second rank galaxy in each FG.

Fig. 11c compares the  $\delta_N$  distributions of FGs and field galaxies. Since we do not have second rank galaxies for the field sample, we obtained the corresponding density excesses as follows. For each field galaxy with apparent and absolute magnitudes  $m_r$  and  $^{0.1}M_r$ , we randomly assign a magnitude shift  $\Delta M$  following the distribution of magnitude differences between first and second rank galaxies of the 102 FG candidates (see Fig. 12). Then, we set  $m_2 = m_r + \Delta M$ , and measure the density excess around the field galaxy following the procedure out-

<sup>12</sup> This is defined as 95% detectability for point-like sources.

lined above. In other words, we assign a fictitious *second rank* galaxy to each field galaxy according to the magnitude distribution of first and second rank galaxies in the sample of 102 FG candidates. Fig. 11c shows that most galaxies in each sample tend to have positive  $\delta_N$  values. In fact, as shown in Tab. 1, the mean value of the density excess is about 2.5 for both samples, and, considering the corresponding uncertainty, is always significantly larger than zero. This implies that there is an excess of faint galaxies in the surrounding regions of both FG and field galaxies. Both Fig. 11c and the mean and width values reported in Tab. 1 show that the distributions of  $\delta_N$  values of FG and field galaxies are fully consistent.

## 6. FGS AND THE RED SEQUENCE

The distribution of FG seed galaxies in color-magnitude space can provide clues to their formation history. We characterize the  $g-r$  vs.  $r$  color-magnitude relation of early-type galaxies as described in App. B, and then compare the distribution of FG and field galaxies to that relation. It is implicit in this simple analysis that the red sequence mainly originates from a mass-metallicity relation (see e.g. Kodama et al. 1998), and that galaxies lying on the sequence represent, as a first approximation, passively evolving systems that have not experienced recent episodes of star formation. By measuring how distant the colors of FGs are from the color-magnitude relation, we have an indication of how star formation is evolving in these systems.

We compute the distance  $\delta_{CM}$  of the colors of FG and field galaxies to the red sequence as

$$\delta_{CM} = \frac{[(g-r) - (a + b \times 0.1M_r)]}{\sigma_{g-r}(0.1M_r)}, \quad (3)$$

where  $a$  and  $b$  are the offset and slope of the color-magnitude relation, and  $\sigma_{g-r}(0.1M_r)$  is the scatter about the red sequence (see Eq. B1 of Appendix B). Fig. 11d compares the  $\delta_{CM}$  distribution of FG and field samples, with the corresponding mean and width values tabulated in Tab. 1. The results of the KS test, comparing the  $\delta_{CM}$  distributions, is also reported in the same table. We see that the  $\delta_{CM}$  distributions are always peaked near zero, as one would expect since FGs and field galaxies are morphologically selected as early-type systems. Fig. 11d suggests that field galaxies have a broader distribution than FGs. However, the corresponding mean values are fully consistent with zero and their widths are consistent with unity, implying no significant difference between the  $\delta_{CM}$  distributions. This result is also confirmed by the p-value from the KS test.

## 7. STRUCTURAL PROPERTIES AND COLOR GRADIENTS

We analyze the surface brightness distribution of FG seed galaxies by studying (i) their structural parameters and internal color gradients, and (ii) the departures of galaxy isophotes from purely elliptical shapes. Internal color gradients are estimated using the structural parameters of galaxies, specifically the effective radius,  $r_e$ , and the Sersic index (shape parameter),  $n$ , while galaxy isophotes are characterized using the  $a_4$  parameter that describes boxy/disky departures of the isophotes from elliptical shapes (Bender & Möllenhoff 1987). The derivation of these quantities is described in App. C.

Figs. 11e and 11f compare the distributions of effective radii and shape parameters for FG and field galaxies. The mean and width values of FGs and the field sample (see Tab. 1) are fully consistent, with the p-values of the KS tests greater than  $\sim 0.2$ . The lack of galaxies with Sersic index  $n \gtrsim 2$  is a natural consequence of our sample consisting of morphologically selected early-type galaxies. Although the Sersic index does not provide a precise measurement of the bulge to disk ratio of a galaxy, it can effectively separate disk and bulge dominated systems, with  $n \sim 2$  as the dividing value between the two classes (e.g. Blanton et al. 2005).

Fig. 11g compares the distributions of color gradients,  $\nabla(g-r)$ , for FG and field galaxies. We find that fossils and field galaxies have a consistent mean color gradient of  $\nabla(g-r) \sim -0.07$ , but the scatter of field galaxies around the mean value is somewhat larger than that of FGs (see Tab. 1). The difference between the width values of the two samples is  $0.16 \pm 0.1$ , which is (marginally) greater than zero by  $1.6\sigma$ . The KS test (Tab. 1) confirms that there is no significant difference between the two samples. Our color gradient estimates can be directly compared with those of La Barbera et al. (2005), who derived the mean  $g-r$  color gradient in early-type galaxies in clusters of different richnesses at different redshifts. For galaxies in poor groups at a redshift of  $z \sim 0.08$ , close to the median redshift of our FG and FS samples, they found a mean color gradient of  $-0.064^{+0.008}_{-0.02}$  (see their Tab. 1), agreeing with the mean  $\nabla(g-r)$  values reported in Tab. 1. The mean value of  $\nabla(g-r)$  has also been measured from SDSS data by Wu et al. (2005), who analyzed a sample of 36 early-type galaxies at  $z \sim 0.02$ . They find a mean  $\nabla(g-r)$  value of  $-0.05 \pm 0.01$  (see their Tab. 3), which differs by less than  $2\sigma$  from the results in Tab. 1.

In Fig. 11h, we compare the distributions of  $a_4$  values for FG and field galaxies. Looking at the mean and width values reported in Tab. 1 as well as at the KS test results reported in Tab. 1, the distributions for FG, and field galaxies are again fully consistent. The distribution of  $a_4$  values carries interesting clues about the formation of FG galaxies. Analyzing the isophotal shapes of seven FG galaxies drawn from the sample of Jones et al. (2003), Khosroshahi et al. (2006, hereafter KPJ06) found that all FG galaxies tend to have disk isophotes. In more detail, examining Fig. 3, three (of seven) FGs in the KPJ06 sample have  $a_4$  values very close to zero, with the remaining four galaxies having significantly larger values. In our sample, we find that the distribution of FGs is peaked around  $a_4 = 0$ , with equal numbers of disk and boxy systems. The disagreement we find with KPJ06 may reflect the small sample analyzed in that study. Our comparison of FG and field galaxies shows no difference in isophotal deviations from elliptical shapes. In other words, FG galaxies do not have peculiar isophotes when compared to ‘normal’ field galaxies.

## 8. STELLAR POPULATIONS

To analyze the stellar populations of FGs and field galaxies, we use spectra from the SDSS-DR4 with a resolution of  $4.42 \text{ \AA}$  (FWHM). For each galaxy, we search for the Single Stellar Population (SSP) model that best matches the galaxy spectrum. The matching is performed using measurements of spectral indices, resulting

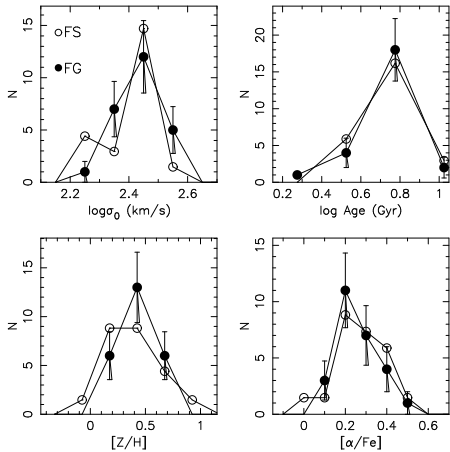


FIG. 13.— Same as Fig. 11 but comparing velocity dispersions and stellar population parameters for FG and field galaxies.

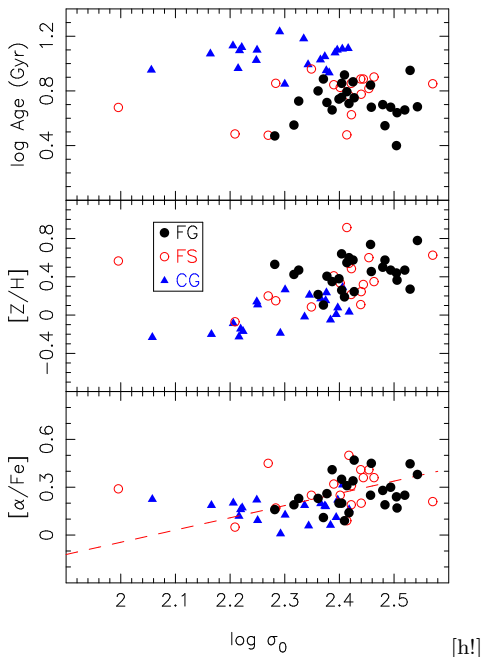


FIG. 14.— Correlations of stellar population parameters with velocity dispersion for FGs, field galaxies, and galaxies in Hickson Compact Groups, represented with different symbols as shown from the inset in the middle panel. In the bottom figure, as an aid to the discussion, the best fit to the sample of sixty-six field galaxies (see Sec. 3) is plotted (dashed line). Values of stellar population parameters from the de la Rosa et al. (2007) have been transformed to the  $\alpha$ -models system used here (see App. D).

in estimates of age, metallicity, and elemental abundance ratios  $[\alpha/\text{Fe}]$ . The procedure consists of (i) estimating the spectral indices, and (ii) extracting the stellar population parameters, as detailed in App. D.

Velocity dispersions and stellar population parameters for FGs and field galaxies are reported in Tab. 2. The distributions of  $\sigma$ , age,  $[Z/\text{H}]$ , and  $[\alpha/\text{Fe}]$  are shown in Fig. 13, with the corresponding mean and width values, and the KS test being reported in Tab. 1. We see that the distributions of FGs and field samples are fully consistent, with the p-value of the KS test being larger than

$\sim 0.1$ . Fig. 14 shows how stellar population parameters vary as a function of velocity dispersion for both FGs and field galaxies. We see that both samples follow the same correlation between  $[\alpha/\text{Fe}]$  and velocity dispersion, as found from previous studies for field galaxies (e.g. de la Rosa et al. 2007). Moreover, both FGs and field galaxies occupy the same region in the diagrams of age and metallicity versus velocity dispersion, emphasizing the similarity of both samples. In Fig. 14, we also insert the stellar population parameters for the twenty elliptical galaxies in Hickson compact groups (HCGs) analyzed by de la Rosa et al. (2007). The stellar population parameters of these galaxies were remeasured following the same procedure as for FGs and field galaxies. Note that ellipticals in HCGs have higher ages and lower metallicities than both FGs and field galaxies, showing no correlation between  $[\alpha/\text{Fe}]$  and velocity dispersion.

## 9. DISCUSSION

In the current hierarchical model of galaxy formation, the basic idea is that massive galaxies form later as the result of the merging history of their dark matter halos, but their stars form earlier (downsizing). In this sense special attention is being focused on massive (luminous) galactic systems, whether they reside in low or high density locations. We may find fossils at different cosmic epochs, and they provide important clues that help us distinguish between nature and nurture. Our main results from this paper are:

We found 578 candidates following our optical photometric definition of FGs in the redshift range  $0.05 < z < 0.095$ . After discarding incorrect morphological classifications and AGN we are left with 102 FGs for which there is a significant X-ray detection in ROSAT (maximum total flux of  $10^{-14} \text{erg cm}^{-2} \text{s}^{-1}$ ). Only twenty-five FGs were selected with likely extended X-ray emission and not associated with rich clusters. These constitute our final sample of FGs. Applying the  $V/V_{\text{max}}$  test we find a spatial density of  $2.83 \times 10^{-6} h_{75}^3 \text{Mpc}^{-3}$ , comparable to three other independent observational studies (V99, RO00, and JO03) and to the recent analysis of the Millennium Simulation by Dariush et al. (2007).

As shown in Figure 12, the brighter FGs always have  $\Delta M$  greater than  $\sim 3.0$  mag while fainter FGs are limited by the completeness of the SDSS catalog. The lack of systems in the lower left part of the figure, at magnitudes brighter than  $0.1 M_r \sim -23$ , might be caused by selection effects as well as by the shape of the galaxy LF. Thus, it is not clear from the present analysis if the absence of systems in the lower left part of Fig. 12 is related to some physical characteristics of the sample. It would be reasonable to expect that as mergers progress the LF of such systems will have a larger gap between the first and the second ranked galaxies.

The density excess around FGs is fully consistent with what we measure for field galaxies, implying that the environments around both systems are statistically identical when considering the faint galaxy population. This result seems to indicate that FGs and field galaxies originate from similarly overdense regions of the Large Scale Structure.

By studying the distribution of color offsets from the red sequence, we find that FGs occupy a similar region to field ellipticals. We also find that the mean color gra-

dients in both samples (FG and FS) are statistically the same. However, the scatter around the mean for FGs is significantly ( $1.6 \sigma$ ) smaller than that for field ellipticals, which may indicate a more regular process in the buildup of FGs, such as mergers of  $L^*$  galaxies. The distribution of  $a_4$ , which measures isophotal shape deviations from a pure ellipses, indicates that FGs and field ellipticals are similar.

Studying the stellar populations in the twenty-five FGs and seventeen field galaxies we find that there is no difference in age, metallicity or  $\alpha$ -enhancement, indicating that the star formation history of fossil groups seems to be analogous to that of field ellipticals. We further examined elliptical galaxies in compact groups studied by de la Rosa et al. (2007). As already established in previous works, elliptical galaxies in CGs are older and more metal-poor than field ellipticals (Proctor et al. 2004; de la Rosa et al. 2007) and fossil groups. Particularly, when we look at the relation between  $[Z/H]$  and  $\log \sigma$ , the mass-metallicity relation is evident (see Lee et al. 2006; Kobayashi 2005). More massive galaxies (in both FGs and field galaxies) retain their metals more efficiently than the low mass ones (i.e., ellipticals in CGs). The  $\alpha$ -enhancement diagram shows a clear trend between  $\alpha/F_e$  and velocity dispersion (mass). This can be interpreted as a manifestation of downsizing - the less massive galaxies have a more extended star formation history. Based on these results we see that FGs are similar to field ellipticals but cannot be formed by dry mergers of ellipticals in a CG. However, a wet merger with a gas rich disk system may also explain the observed relations. Here, the luminosity-weighted parameters (Age,  $[Z/H]$ ,  $[\alpha/Fe]$ ) are more sensitive to the recent star-formed-population, generating lower ages, higher  $[Z/H]$  and higher  $[Mg/Fe]$ . This assumes that the merger-starburst is soon followed by SN/AGN feedback which depletes the gas content.

McCarthy et al. (2004) have found a significant pop-

ulation of red galaxies at high redshift ( $1.3 < z < 2.2$ ), and claim that they cannot be descendants of the  $z \sim 3$  Lyman-break galaxies. Based on their spectroscopic data they also conclude that most of the present day massive galaxies had an early ( $z_f = 2.4$ ) and rapid formation. If we restrict ourselves to the twenty-five FGs, their last main star formation episode must have occurred at  $z > 0.3$ , much more recently than in the high- $z$  galaxies. It appears that a more recent burst occurred in the FGs which would explain their lower ages. Therefore, we may be seeing massive ellipticals that accreted a small galaxy at  $z > 0.3$ .

Our results indicate that FGs are not significantly different from bright ellipticals found in low-density regions of the universe. As claimed by Mulchaey & Zabludoff (1999) in a detailed study of NGC 1132, FGs could simply be "failed" groups - a few relatively bright galaxies merged forming the dominant system we see today, but without enough surrounding matter to form additional nearby bright galaxies, resulting in an atypical LF. This is also in agreement with recent results obtained by D'Onghia et al. (2005) based on N-body/hydrodynamical cosmological simulations where they find that FGs are formed by the infall of  $L \sim L_*$  systems along filaments with impact parameters as small as 5 kpc.

Our findings suggest that the objects meeting the observational criteria expected for fossil groups at low redshift might not be true fossils. The extensive study presented here whereby we select FG candidates based on optical data, and then examining their X-ray counterparts reveals no difference between FGs and field ellipticals. We note that fossils can be created anytime in cosmic history, and these systems may represent the final stage of mass assembly as suggested in the analysis of the Millennium simulation by Dariush et al. (2007), instead of forming a distinct class.

## APPENDIX

### LIST OF PROPERTIES OF FGS AND FIELD GALAXIES

Tab. 2 lists all the quantities used to characterize the samples of FGs and field galaxies. FGs with extended X-ray contours ( $N = 25$ ) have flag=1 in column 21, while field galaxies ( $N = 17$ ) have flag=2. The table also lists the four FG candidates that are not in the final FG sample because they do not fulfill the X-ray extension criterion. These objects have flag=0. Column 1 is a running number for the list of FGs and field galaxies. Columns 2, 3, and 4 give the RA and DEC (in degrees) and spectroscopic redshift from the SDSS DR4. Columns 5, 6, and 7 provide the  $z = 0.1$  k-corrected absolute magnitude, the magnitude gap of the FG, and the  $g - r$  color, respectively. For field galaxies, the values of  $\Delta M$  have been randomly assigned as described in Sec. 4. Column 8 provides the density excess around each galaxy. Columns 9 and 10 report the effective radii (in arcsec) in the  $g$  and  $r$  bands, while columns 11, and 12 list the corresponding Sersic indices. Columns 13 and 14 provide the  $a_4(\times 100)$  parameters and internal color gradients (in mag/dex). Column 15 reports the X-ray luminosity in units of  $10^{44} h_{75}^{-2} \text{erg/s}$ . Column 16 provides the distance of each galaxy to the red sequence (Eq. 3). Columns 17 to 20 provide the velocity dispersions (in units of km/s) and stellar population parameters.

### MEASURING THE RED SEQUENCE

To quantify the properties of the FG first-rank galaxies relative to the red sequence, we use the SDSS-DR4 galaxy catalog to calculate the offset, slope and scatter of the  $g - r$  vs.  $r$  color-magnitude relation for all early-type galaxies. Following a procedure similar to Bernardi et al. (2003), we select early-type galaxies on the basis of the SDSS spectroscopic parameter *eclass*, which classifies the spectral type using a principal component analysis, and the photometric parameter *fracDev<sub>r</sub>*, which measures the fraction of the galaxy light distribution that is better fit by a de Vaucouleurs law. We define as early-type galaxies those systems with *eclass* < 0 and *fracDev<sub>r</sub>* > 0.8, resulting in a sample of 39733 (out of 91563) galaxies selected from the SDSS catalog used to search for fossil systems (see Sec. 2.1). Total galaxy magnitudes are taken from the  $r$ -band Petrosian magnitudes output by the SDSS photometric pipeline, since they are model-independent and highly reliable for bright galaxies. Colors are obtained from the  $g$  and  $r$  band SDSS model

magnitudes because they are measured in the same aperture for all filters. Both magnitudes and colors are k-corrected using the *kcorrectv4\_1.4* software package (Blanton et al. 2003), allowing k-corrections to be estimated through filters that are blue-shifted by a factor  $(1 + z_0)$ . This procedure has the primary advantage of minimizing uncertainties on k-corrections, provided that the value of  $z_0$  is close to the redshift range of the observed galaxies. Following other papers that analyze the color and magnitude distribution of galaxies in the SDSS database (e.g. Hogg et al. 2004), we choose  $z_0 = 0.1$ , corresponding to the upper redshift limit of our galaxy catalog, and we indicate the  $z_0 = 0.1$  k-corrected model magnitudes with  $^{0.1}g$  and  $^{0.1}r$ , and the  $z_0 = 0.1$  k-corrected Petrosian absolute magnitude with the notation  $^{0.1}M_r$ .

Fig. 15 shows the color–magnitude diagram of both early-type and all galaxies in our catalog. Although the catalog is almost complete down to  $M_r = -20$  (see Sec. 2.1), we note that the difference in k-corrections for galaxies with  $M_r \sim -20^{13}$  makes the color–magnitude diagram incomplete down to that magnitude limit. Therefore, we derive the slope,  $a$ , and the offset,  $b$ , of the color–magnitude relation by minimizing the rms of galaxy colors around the linear relation, using only galaxies brighter than  $M_r \sim -20.2$ . To reduce the effect of outliers, the color rms is computed via bi-weight statistics (Beers et al. 1990). The uncertainties on  $a$  and  $b$  are estimated through the bootstrap method, with  $N = 1000$  bootstrap iterations. For the sample of early-type galaxies, we find  $a = 0.944 \pm 0.005$  and  $b = -0.0206 \pm 0.003$ , consistent with  $b = -0.022$  reported by Hogg et al. (2003) and with other results in the literature (e.g. Cool et al. 2006; Gallazzi et al. 2006). The derived values of  $a$  and  $b$  change by less than 10% if we apply the same fitting procedure to the entire galaxy catalog (i.e. not applying the *eclass* and *fracDev<sub>r</sub>* cuts), demonstrating the robustness of the regression method. To estimate the scatter around the color–magnitude relation, we bin the sample of early-type galaxies with respect to magnitude, and derive the color rms,  $\sigma_{g-r}$ , in each bin with bi-weight statistics. Fig. 16 plots  $\sigma_{g-r}$  as a function of  $^{0.1}M_r$ . We find that  $\sigma_{g-r}$  increases at the faintest magnitudes, with this trend well-fit by the relation

$$\sigma_{g-r}(^{0.1}M_r) = 0.045 - 0.00047 \times (^{0.1}M_r + 20.2)^4, \quad (\text{B1})$$

in the magnitude range  $-23 < ^{0.1}M_r < -20.2$ . The mean value of  $\sigma_{g-r}$  is 0.035, consistent with that found in previous

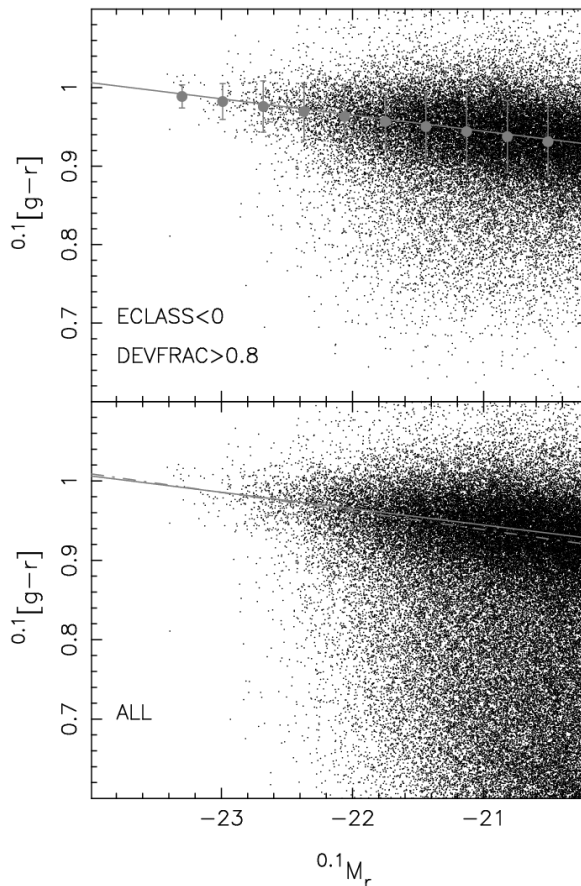


FIG. 15.— Color–magnitude diagram of early-type galaxies (upper panel) and of all galaxies (lower panel) in the catalog. The grey line in the upper panel shows the bi-weight fit to the data, while grey circles, and error bars plot the mean and standard deviation,  $\sigma_{g-r}$ , of the color distribution in different magnitude bins. The grey solid line in the lower panel is the same as that in the upper panel, while the grey dotted line shows the bi-weight fit to the color–magnitude relation of all galaxies in the catalog.

<sup>13</sup> As mentioned in Sec. 5, k-corrections have not been applied when computing total magnitudes to select the SDSS-DR4 catalog.

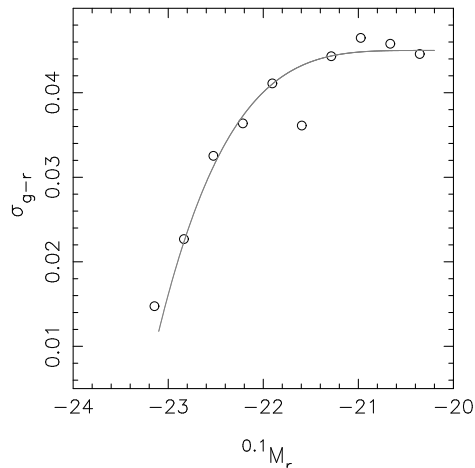


FIG. 16.— The scatter around the red sequence,  $\sigma_{g-r}$ , plotted as a function of central value of each magnitude bin in the upper panel of Fig. 15. The grey curve is the polynomial fit to the points, as given in Eq. B1.

studies (see e.g. Cool et al. 2006).

#### MEASURING STRUCTURAL PARAMETERS AND INTERNAL COLOR GRADIENTS

Structural parameters were derived using 2DPHOT (La Barbera et al. 2008, hereafter LdC08), an automated software environment that performs several tasks, such as catalog extraction (using S-Extractor, Bertin & Arnouts 1996), star/galaxy separation, and surface photometry. To estimate color gradients, structural parameters were measured in both the  $g$  and  $r$  bands. For each galaxy in the FG and field (FS) samples we retrieved the corresponding  $g$ - and  $r$ -band *corrected frames* from the SDSS DR4 Data Archive Server and ran 2DPHOT on them. A complete description of the 2DPHOT package can be found in LdC08; here we provide a brief description of the steps relevant to measuring galaxy structural parameters. For each galaxy, a PSF model was constructed by fitting the four closest stars in the image with a sum of three two-dimensional Moffat functions. Isophotal distortions of star isophotes were modeled as described in LdC08. The parameters  $r_e$ ,  $\langle \mu \rangle_e$  and  $n$  were then obtained by fitting galaxy images with PSF-convolved Sersic models. As an example of the fitting procedure, Fig. 17 plots the images of a subset of galaxies from the list of twenty-five FGs, along with the residuals after subtracting the best-fitting Sersic models. The shapes of FG and FS candidates are characterized by the isophotal shape parameter,  $a_4$ , of each galaxy. Isophotal contours were expanded into a  $\sin/\cos$  series (Bender & Möllenhoff 1987), and analyzed as described in LdC08, by deriving the  $a_4$  coefficient as the average of the  $a_4$  profile within a radial range from four times the FWHM to twice the galaxy effective radius.

Internal color gradients, defined as the logarithmic slope of the galaxy radial color profile, were estimated as follows (see also La Barbera et al. 2003). For each galaxy in the FG and FS samples, the corresponding  $g$ - and  $r$ -band best-fitting Sersic parameters were used to construct seeing-deconvolved galaxy images. A set of concentric ellipses were constructed for both the  $g$ - and  $r$ -band galaxy images, with all ellipses having the same position angle and axis ratio parameters as those derived from the  $r$ -band Sersic fitting (Sec. C). For each ellipse, a  $g-r$  color was calculated as the average ratio of the  $g$ - and  $r$ -band intensity values along that ellipse. The color profile was then computed as the average  $g-r$  color as a function of the equivalent radius of the corresponding ellipse. An ordinary least-squares fit to the color profile, adopting the color index as the independent variable, was then performed, with the slope of the fitted line yielding the internal color gradient for each galaxy. Following previous studies of color gradients in early-type galaxies (e.g. Peletier et al. 1990), the fit was performed in a range of the color profile, from an inner radius of 0.1 to an outer radius of 1.0 times the  $r$ -band effective radius.

#### SPECTRAL ANALYSIS

##### *Measuring spectral parameters*

The spectra of FGs and field galaxies were masked to avoid bad pixels affecting the wavelength ranges defining the spectral indices, brought to redshift zero and corrected for foreground dust extinction following Schlegel, Finkheiner & Davis 1998. Then, we derived the spectral indices  $H\beta$ ,  $[MgFe]' = (Mgb (0.72 \times Fe5270 + 0.28 \times Fe5335))^{1/2}$ ,  $Fe3 = (Fe4383+Fe5270+Fe5335)/3$ , and  $jFe_i = (Fe5270+Fe5335)/2$ , which are defined according to the Lick system (Worthey & Ottaviani 1997; González 1993), except for the higher resolution of the SDSS spectra.

The measurement of the  $H\beta$  spectral index, which is directly related to age, may be significantly affected by nebular emission, biasing the inferred age towards older values. To correct for this effect, we used the STARLIGHT code (Cid Fernandes et al. 2005) which finds the best fit to the observed spectrum by combining a set of SSP-MILES Spectral Energy Distributions (SEDs; see Sec. 8.2), convolved to the SDSS spectral resolution and broadened to match the galaxy's velocity dispersion. As a result of the fitting procedure, STARLIGHT also provides the velocity dispersion,  $\sigma$ , of each galaxy. During the fitting process, regions around emission lines were masked. Fig. 18 shows how the residual

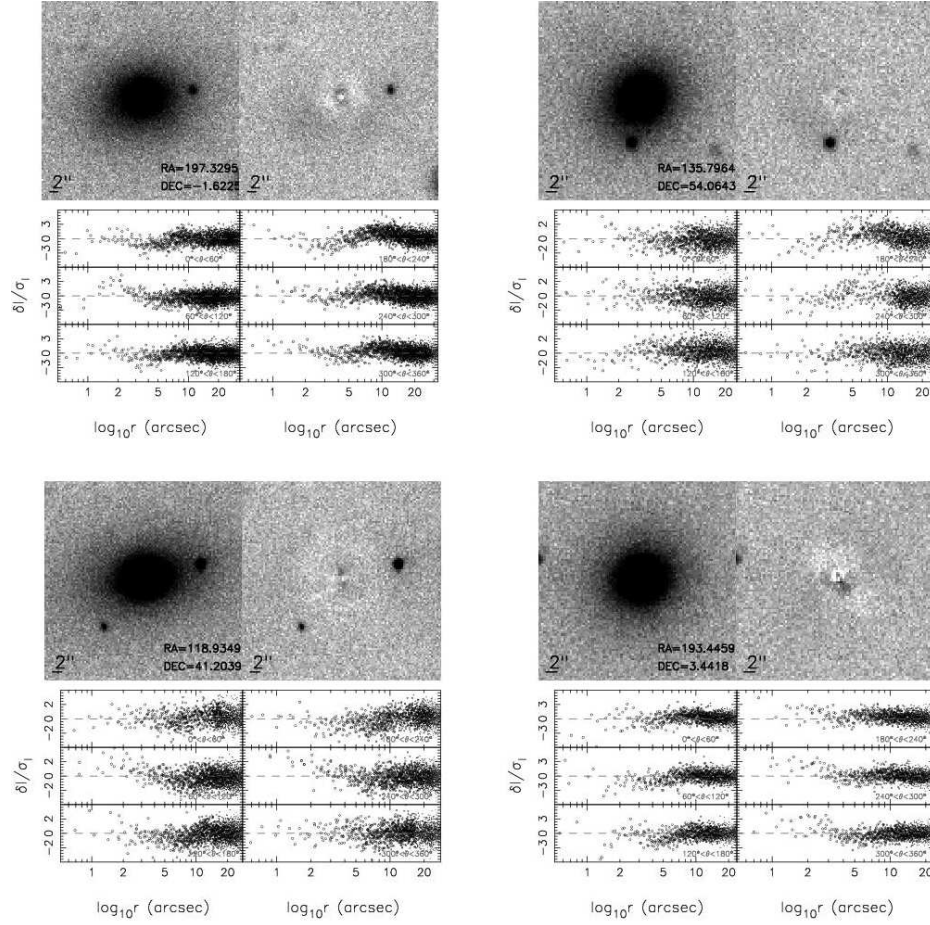


FIG. 17.— Two-dimensional fitting of four galaxies drawn from the sample of twenty-five FGs. For each galaxy, the upper-left and right subpanels show the galaxy  $r$ -band image and the corresponding residual map after model subtraction, respectively. Right ascension and declination are reported, in degrees, in the lower right corner of the left subpanel. The spatial scale is shown in the lower-left corners. The lower six subpanels show the fitting residuals, normalized to the photon noise in each pixel, as a function of the radial distance,  $r$ , to the galaxy center within six bins of the polar angle,  $\theta$ , respectively. The limits of each bin are shown in the lower right corner of each subpanel.

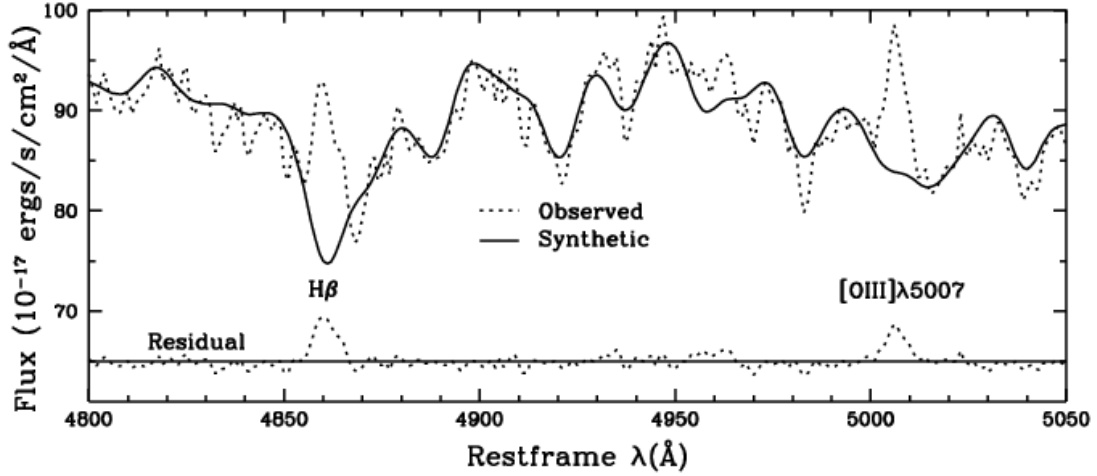


FIG. 18.— The synthetic spectrum obtained by STARLIGHT (continuous line) is the combination of SSP models which best fits the observed SDSS-spectrum (dotted line). The residual spectrum (observed – synthetic), can be used to measure emission indices. Instead of correcting for emission filling, we measure the  $H\beta$  index directly from the synthetic spectrum

spectrum unveils the nebular emission. Instead of correcting for the residual emission line, we measured the  $H\beta$  index directly from the absorption spectra obtained by STARLIGHT.

Velocity dispersions of FGs and field galaxies were taken from the SDSS DR4. For 53 galaxies (out of 102 FG candidates and 66 field galaxies with significant X-ray detection), the  $\sigma$  measurements were not available from the SDSS database, and in this case we adopted the STARLIGHT estimates. The spectral parameters, i.e., velocity dispersions and spectral indices, were corrected to a common physical aperture of  $R_{eff}/8$ , following Jørgensen et al. (1995) and Jørgensen (1997). For each galaxy, the effective radius,  $R_{eff}$ , was defined as  $R_{eff} = (b/a) \times R_{dev}$ , using the  $deV Rad_r$  ( $R_{dev}$ ) and  $deV AB_r$  ( $b/a$ ) parameters from the SDSS database. Since the aperture corrections rely on effective radii derived by fitting de Vaucouleurs models, we adopted the SDSS photometric pipeline's  $R_{eff}$  values, instead of using our effective radii derived using Sersic models (see App. C).

#### *Extraction of stellar population parameters*

We measured age, metallicity and abundance ratio  $[\alpha/Fe]$  using the recently developed  $\alpha$ -enhanced SSP-MILES models (de la Rosa et al. 2008), which provide SEDs at 2.4 Å (FWHM) resolution for different  $\alpha$ -enhancement ratios, combining theoretical (Coelho et al. 2005) and empirical (MILES) libraries (Sánchez-Blázquez et al. 2006). For each galaxy, we constructed a grid of  $H\beta$  and  $[MgFe]'$  values using the solar metallicity SSP models ( $[\alpha/Fe]=0$ ) with a variety of age and  $[Z/H]$  combinations. The age and  $[Z/H]$  of the observed spectrum were obtained by interpolating its two spectral indices among those of the models. The  $H\beta$  and  $[MgFe]'$  indices are mostly sensitive to age and metallicity, respectively, breaking the well-known age-metallicity degeneracy. Moreover, they have the advantage of being almost insensitive to  $[\alpha/Fe]$  (Korn, Maraston & Thomas 2005). As a second step, after fixing the estimated age, we construct a new grid of Fe3 and Mgb values with models having a variety of  $[Z/H]$  and  $[\alpha/Fe]$  combinations. Interpolation of the observed indices yields the final metallicity and  $[\alpha/Fe]$  values. To check the reliability of the  $\alpha$ -enhancement estimates, we repeated the above computation, replacing the Fe3 index with  $\langle Fe \rangle = (Fe5270 + Fe5335)/2$ . The two procedures are fully consistent at a confidence level of  $2\sigma$  for all but three of the FG and FS galaxies. For those three objects, we adopted the more accurate  $\langle Fe \rangle$  estimate (see de la Rosa et al. 2008).

We thank the referee for several comments that helped to significantly improve this paper. We acknowledge Dr. D.Kocevski for helping us with X-ray analysis of the RASS data. G.S. and A.R. thank the EC and the MIUR for having partially supported this work (EC contracts HPRN-CT-2002-00316 - SISCO network, and MIUR-COFIN-2004 n.2004020323\_001).

Funding for the SDSS and SDSS-II has been provided by the Alfred P. Sloan Foundation, the Participating Institutions, the National Science Foundation, the U.S. Department of Energy, the National Aeronautics and Space Administration, the Japanese Monbukagakusho, the Max Planck Society, and the Higher Education Funding Council for England. The SDSS is managed by the Astrophysical Research Consortium for the Participating Institutions. The Participating Institutions are the American Museum of Natural History, Astrophysical Institute Potsdam, University of Basel, Cambridge University, Case Western Reserve University, University of Chicago, Drexel University, Fermilab, the Institute for Advanced Study, the Japan Participation Group, Johns Hopkins University, the Joint Institute for Nuclear Astrophysics, the Kavli Institute for Particle Astrophysics and Cosmology, the Korean Scientist Group, the Chinese Academy of Sciences (LAMOST), Los Alamos National Laboratory, the Max-Planck-Institute for Astronomy (MPA), the Max-Planck-Institute for Astrophysics (MPIA), New Mexico State University, Ohio State University, University of Pittsburgh, University of Portsmouth, Princeton University, the United States Naval Observatory, and the University of Washington.

#### REFERENCES

- Adami, C., et al. 1998, A&A, 336, 63  
 Anderson, S.F., et al. 2007, AJ, 133, 313  
 Avni, Y., & Bahcall, J.N. 1980, ApJ, 235, 694  
 Barnes, J.E. 1989, Nature, 338, 123  
 Bajaja, E., et al. 2005, A&A, 440, 767  
 Beers, T.C., Flynn, K., & Gebhardt, K. 1990, AJ 100, 32  
 Bender, R., & Möllenhoff, C. 1987, A&A, 177, 71  
 Bernardi, M., et al. 2003, AJ, 125, 1817  
 Bertin, E., & Arnouts, S. 1996, A&AS, 117, 393  
 Beuing, J., et al. 1999, MNRAS, 302, 209  
 Blanton, M.R., et al. 2003, AJ, 125, 2276  
 Blanton, M.R., et al. 2005, ApJ, 629, 143  
 Böhringer, H., et al. 2000, ApJS, 129, 435  
 Cid Fernandes, R., et al. 2005, MNRAS, 358, 363  
 Coelho, P., et al. 2005, A&A, 443, 735  
 Cool, R.J., et al. 2006, AJ, 131, 736  
 Dariush, A., et al. 2007, MNRAS, 382, 433  
 de Grandi, S. et al. 1997, ApJ, 486, 738  
 de la Rosa, I.G., et al. 2007, AJ, 133, 330  
 de la Rosa, I.G. et al. 2008, in preparation  
 Evvard, A.E., et al. 1996, ApJ, 469, 494  
 Gal., R.R., et al. 2003, AJ, 125, 2064  
 Gallazzi, A., et al. 2006, MNRAS, 370, 1106  
 Gómez, P.L., et al. 2003, ApJ, 584, 210  
 González, J.J. 1993, PhD Thesis (University of California, Santa Cruz), 172  
 Hausman, M.A., & Ostriker, J.P. 1978, ApJ, 224, 320  
 Hogg, D.W., et al. 2003, ApJ, 585, 5  
 Hogg, D.W., et al. 2004, ApJ, 601, 29  
 Jones, L.R., et al. 2000, MNRAS, 312, 139  
 Jones, L.R., et al., 2003, MNRAS, 343, 627  
 Jørgensen, I. 1997, MNRAS288, 161  
 Jørgensen, I., Franx, M., & Kjærgaard, P. 1995, MNRAS, 276, 1341  
 Kewley, L.J., et al. 2006, MNRAS 372, 961  
 Khosroshahi, H.G., Jones, L.R., Ponman, T.J. 2004, MNRAS, 349, 1240  
 Khosroshahi, H.G., Ponman, T.J., Jones, L.R. 2006, MNRAS, 372, 68  
 Khosroshahi, H.G., Ponman, T.J., & Jones, L.R. 2007, MNRAS, 377, 595  
 Kobayashi, C. 2005, MNRAS, 361, 1216  
 Kodama, T., et al. 1998, A&A, 334, 99  
 Komossa, S., Böhringer, H., and Huchra, J.P. 1999, A&A, 349, 88



- Korn, A.J., Maraston, C., Thomas, D. 2005, A&A, 438, 685  
La Barbera, F., et al. 2003, A&A, 409, 21  
La Barbera, F., et al. 2005, ApJ, 626, 19L  
La Barbera, F., et al. 2008, PASP, 120, 681  
Lee, H., et al. 2006, ApJL, 647, 970  
McCarthy, P.J., et al. 2004, ApJ, 614, 9  
Mulchaey, J.S., and Zabludoff, A.I. 1999, ApJ, 514, 133  
D'Onghia, E.D., et al. 2005, ApJL, 630, 109  
Peletier, R.F., et al. 1990, AJ, 100, 1091  
Ponman, T.J., et al. 1994, Nature, 369, 462  
Ponman, T.J., & Bertram, D. 1993, Nature, 363, 51  
Proctor, R.N., et al. 2004, MNRAS, 349, 1381  
Raymond, J.C., & Smith, B.W. 1977, ApJS, 35, 419  
Romer, A.K. et al. 2000, ApJS, 126, 209  
Sanchez-Blazquez, P. et al. 2006, MNRAS, 371, 703  
Santos, W.A., Mendes de Oliveira, C., Sodr e, L.J. 2007, AJ, 134, 1551  
Schlegel, D., Finkbeiner, D.P., & Davis, M. 1998, ApJ, 500, 525 (SFD98)  
Sorrentino, G., Antonuccio-Delogu, V., Rifatto, A. 2006, A&A, 460, 673  
Sthoughton, C., et al. 2002, AJ, 123, 485  
Sun, M., et al. 2004, ApJ, 612, 805  
Tozzi, P. et al. 2006, A&A, 451, 457T  
Ulmer, M.P., et al. 2005, ApJ, 624, 124  
Vikhlinin, A., et al. 1999, ApJ, 520, 1  
Voges, W. et al. 1999, A&A, 349, 389  
Worthey, G. & Ottaviani, D.L. 1997, ApJS, 111, 377  
Wu, H., et al. 2005, ApJ, 622, 244  
Yoshioka, T., et al. 2004, AdSpR, Vol.34, 12, p.2525

TABLE 2  
PROPERTIES OF FG AND FS GALAXIES.

ID (1)	R.A. (2)	Dec (3)	z (4)	$^{0.1}M_r$ (5)	$\Delta M$ (6)	$^{0.1}g-r$ (7)	$\delta_N$ (8)	$r_{e,g}$ (9)	$r_{e,r}$ (10)	$n_g$ (11)	$n_r$ (12)	$a_4(\times 100)$ (13)	$\nabla(g-r)$ (14)	$\log L_X$ (15)	$\delta_{CM}$ (16)	$\log \sigma_0$ (17)	$\log Age$ (18)	$[Z/H]$ (19)	$[\alpha/Fe]$ (20)	FLAG (21)
1	197.32954	-1.6225	0.083	-22.917	2.62	1.020	2.6	9.11	8.09	4.1	3.0	0.24	-0.068	0.09	1.894	2.494	0.7	0.47	0.30	1
2	135.79644	54.0643	0.083	-22.663	2.04	0.988	3.0	4.14	5.36	4.0	3.8	-0.20	-0.061	-1.00	0.360	2.479	0.7	0.50	0.28	1
3	118.93488	41.2039	0.074	-22.908	2.35	0.965	3.3	5.66	5.82	5.4	4.5	-0.26	-0.024	-1.05	-0.935	2.404	0.9	0.26	0.20	1
4	193.44587	3.4418	0.066	-22.349	2.41	0.802	-0.8	4.52	4.18	5.4	4.3	0.14	0.042	-0.60	-4.846	2.504	0.4	0.44	0.24	1
5	242.70645	48.3879	0.090	-22.203	1.91	0.956	-0.8	45.14	102.19	8.0	9.8	-0.30	0.093	-0.27	-0.338	2.317	0.6	0.42	0.19	1
6	202.96613	-2.8721	0.086	-22.556	2.34	0.961	3.9	4.49	6.11	5.8	5.5	0.99	-0.041	-0.76	-0.490	2.377	0.7	0.41	0.26	1
7	171.65402	55.3564	0.070	-22.528	1.90	0.960	1.5	300.11	22.26	6.3	4.2	-0.28	-1.155	-0.90	-0.509	2.414	0.8	0.55	0.31	1
8	215.39972	44.7081	0.091	-22.781	2.44	1.006	2.8	26.16	49.60	8.6	8.6	0.97	0.089	-0.80	1.041	2.483	0.5	0.57	0.19	1
9	184.34689	8.8729	0.094	-22.785	2.05	0.952	3.0	37.91	27.49	3.9	3.2	-0.49	-0.487	-0.53	-1.194	2.427	0.7	0.24	0.47	1
10	133.05354	29.4108	0.086	-22.959	2.63	0.970	2.3	13.98	35.33	2.3	3.4	1.29	0.297	-0.76	-0.781	2.399	0.7	0.38	0.20	1
11	216.32744	40.4898	0.083	-22.035	1.97	0.964	-0.0	10.82	12.82	4.8	4.5	0.48	-0.115	-1.70	-0.038	2.326	0.7	0.47	0.23	1
12	191.71340	0.2970	0.089	-23.248	2.94	1.006	4.0	20.44	14.73	7.5	6.0	-0.56	-0.271	-0.65	1.150	2.505	0.6	0.36	0.17	1
13	134.52059	1.1537	0.071	-22.262	1.94	0.997	2.2	26.81	25.39	9.4	9.0	-0.03	-0.108	-1.19	0.727	2.404	0.8	0.64	0.35	1
14	117.99395	20.7490	0.077	-21.775	1.83	0.954	1.3	7.37	8.38	4.5	4.2	1.14	-0.102	-1.04	-0.145	2.282	0.5	0.53	0.16	1
15	9.36782	15.6263	0.080	-22.800	2.42	0.987	2.0	11.72	10.64	6.4	5.1	-0.06	-0.096	-1.15	0.260	2.371	0.9	0.10	0.11	1
16	133.05970	29.3385	0.085	-22.196	1.89	0.993	2.3	8.64	12.85	6.1	6.5	0.15	-0.046	-1.04	0.646	2.457	0.8	0.74	0.25	1
17	325.61206	-6.5868	0.088	-22.750	2.28	0.979	3.4	26.36	35.56	9.9	10.2	2.42	-0.070	-0.93	-0.050	2.409	0.9	0.19	0.09	1
18	358.77843	-9.3756	0.074	-22.516	2.49	0.981	4.2	4.28	4.92	3.6	3.6	0.66	-0.139	-0.98	0.168	2.387	0.7	0.35	0.41	1
19	188.89591	1.8937	0.078	-22.520	2.16	1.025	3.6	37.61	25.27	8.6	7.0	-0.01	-0.223	-1.04	1.568	2.520	0.7	0.47	0.25	1
20	195.28142	-3.4480	0.083	-22.761	2.74	1.007	5.6	10.16	12.72	4.9	4.7	0.46	-0.086	-1.11	1.070	2.425	0.9	0.57	0.34	1
21	354.57353	15.6689	0.066	-22.600	2.68	0.973	1.7	8.45	14.56	2.7	4.0	2.66	0.044	-1.77	-0.122	2.361	0.8	0.21	0.23	1
22	129.81595	28.8441	0.079	-23.281	3.04	0.993	4.6	4.51	6.14	2.1	2.4	0.20	-0.203	-1.10	0.122	2.543	0.7	0.78	0.38	1
23	230.21770	48.6607	0.074	-23.126	3.15	0.943	4.0	10.66	12.67	4.7	4.8	-0.72	-0.102	-0.40	-3.176	2.529	1.0	0.27	0.45	1
24	228.00073	36.6520	0.066	-22.827	2.91	0.980	0.9	11.04	14.23	3.2	3.3	-1.16	0.059	-0.49	-0.078	2.417	0.7	0.60	0.14	1
25	234.78742	33.6881	0.070	-22.555	1.88	1.016	3.8	20.37	20.19	9.9	10.4	0.09	-0.129	-0.84	1.299	2.458	0.7	0.46	0.45	1
26	172.88388	12.6997	0.081	-22.306	1.85	0.972	1.0	7.00	9.99	2.4	2.6	-0.04	-0.108	-1.23	0.017	2.434	0.4	1.46	0.31	0
27	20.09644	-0.0790	0.077	-23.128	3.01	1.003	1.6	32.20	39.10	4.8	5.0	-0.42	-0.133	-1.00	1.110	2.543	0.8	0.40	0.32	0
28	180.40768	1.1980	0.082	-22.225	2.14	0.903	-2.6	10.41	9.42	4.7	9.2	2.29	-0.848	-0.85	-1.773	2.197	0.6	0.09	0.03	0
29	118.18416	45.9493	0.052	-22.167	2.05	0.963	2.3	6.06	5.78	4.5	4.8	-0.45	-0.042	-0.96	-0.144	2.336	0.7	0.23	0.17	0
30	168.84945	54.4441	0.070	-22.802	1.99	0.939	2.6	7.22	7.38	6.3	5.6	-0.89	-0.041	-1.42	-1.795	2.349	1.0	0.09	0.25	2
31	232.31104	52.8640	0.073	-22.927	2.17	0.995	3.2	21.23	24.43	9.8	8.6	-0.34	0.017	-0.36	0.602	2.454	0.8	0.60	0.41	2
32	122.59694	42.2739	0.064	-22.719	2.40	1.013	3.7	4.56	5.02	2.4	2.9	0.10	-0.321	-1.31	1.298	2.571	0.9	0.63	0.21	2
33	184.62019	42.4610	0.073	-22.029	1.93	0.925	-0.4	9.19	9.73	5.1	4.6	-0.05	-0.054	-1.23	-1.015	2.284	0.9	0.15	0.17	2
34	254.08789	39.2752	0.062	-22.595	2.42	0.976	3.2	294.65	50.08	10.7	10.1	-1.20	-0.700	-1.01	-0.038	2.422	0.6	0.48	0.31	2
35	129.46447	26.5988	0.088	-22.705	1.88	0.903	2.2	6.32	8.82	6.2	6.3	-0.39	-0.069	-0.99	-2.875	2.413	0.5	0.92	0.09	2
36	134.49123	30.3439	0.086	-22.817	2.26	0.949	1.2	15.11	14.76	7.4	6.5	-0.10	-0.147	-0.57	-1.422	2.439	0.9	0.11	0.41	2
37	133.51888	29.0535	0.084	-22.938	2.50	1.002	4.6	8.06	13.29	2.9	3.6	1.72	-0.099	-0.49	0.964	2.463	0.9	0.35	0.36	2
38	237.97868	27.8640	0.082	-21.860	1.81	0.979	2.8	8.80	13.18	2.9	4.1	-0.01	-0.327	0.29	0.421	1.996	0.7	0.56	0.29	2
39	136.68638	3.6002	0.072	-22.123	1.90	0.893	-1.5	12.94	21.63	10.9	10.2	0.97	0.146	-0.51	-1.928	2.209	0.5	-0.07	0.05	2
40	144.40096	7.9180	0.093	-21.778	1.75	0.925	-1.3	2.70	4.25	4.2	4.4	0.91	-0.050	-1.40	-0.824	2.270	0.5	0.20	0.45	2
41	141.65320	3.4606	0.088	-22.235	2.15	0.954	3.3	4.45	7.72	4.8	5.9	-0.06	-0.075	-1.24	-0.427	2.422	0.9	0.21	0.19	2
42	178.15655	3.4727	0.081	-22.771	2.22	0.964	3.0	5.71	9.31	1.6	2.9	0.41	-0.625	0.03	-0.665	2.417	0.8	0.54	0.50	2
43	7.36845	-0.2126	0.060	-22.322	1.85	0.981	5.3	4.82	4.83	2.7	2.5	0.47	0.019	-1.35	0.288	2.390	0.8	0.41	0.32	2
44	216.19754	2.6644	0.053	-22.400	1.95	0.961	3.4	7.04	6.69	4.5	4.5	1.04	-0.009	-0.90	-0.344	2.401	0.8	0.34	0.25	2
45	223.93717	-0.3062	0.083	-22.295	1.92	0.905	1.7	1.09	1.49	2.0	2.4	0.91	-0.369	-0.81	-1.818	2.440	0.8	0.24	0.20	2
46	350.73485	-10.0456	0.084	-22.368	2.24	0.989	5.6	4.94	10.10	5.6	7.8	1.13	0.015	-1.10	0.477	2.444	0.9	0.32	0.36	2

Table 2. Properties of FG and FS galaxies.

ID	R.A.	Dec.	z	$^{0.1}M_r$	$\Delta M$	$^{0.1}g-r$	$\delta_N$	$r_{e,g}$	$r_{e,r}$	$n_g$	$n_r$	$a_4(\times 100)$	$\nabla(g-r)$	$\log L_X$	$\delta_{CM}$	$\log \sigma_0$	$\log Age$	[Z/H]	[ $\alpha/Fe$ ]	FLAG
(1)	(2)	(3)	(4)	(5)	(6)	(7)	(8)	(9)	(10)	(11)	(12)	(13)	(14)	(15)	(16)	(17)	(18)	(19)	(20)	(21)
1	197.32954	-1.6225	0.083	-22.917	2.62	1.020	2.6	9.11	8.09	4.1	3.0	0.24	-0.068	0.09	1.894	2.494	0.7	0.47	0.30	1
2	135.79644	54.0643	0.083	-22.663	2.04	0.988	3.0	4.14	5.36	4.0	3.8	-0.20	-0.061	-1.00	0.360	2.479	0.7	0.50	0.28	1
3	118.93488	41.2039	0.074	-22.908	2.35	0.965	3.3	5.66	5.82	5.4	4.5	-0.26	-0.024	-1.05	-0.935	2.404	0.9	0.26	0.20	1
4	193.44587	3.4418	0.066	-22.349	2.41	0.802	-0.8	4.52	4.18	5.4	4.3	0.14	0.042	-0.60	-4.846	2.504	0.4	0.44	0.24	1
5	242.70645	48.3879	0.090	-22.203	1.91	0.956	-0.8	45.14	102.19	8.0	9.8	-0.30	0.093	-0.27	-0.338	2.317	0.6	0.42	0.19	1
6	202.96613	-2.8721	0.086	-22.556	2.34	0.961	3.9	4.49	6.11	5.8	5.5	0.99	-0.041	-0.76	-0.490	2.377	0.7	0.41	0.26	1
7	171.65402	55.3564	0.070	-22.528	1.90	0.960	1.5	300.11	22.26	6.3	4.2	-0.28	-1.155	-0.90	-0.509	2.414	0.8	0.55	0.31	1
8	215.39972	44.7081	0.091	-22.781	2.44	1.006	2.8	26.16	49.60	8.6	8.6	0.97	0.089	-0.80	1.041	2.483	0.5	0.57	0.19	1
9	184.34689	8.8729	0.094	-22.785	2.05	0.952	3.0	37.91	27.49	3.9	3.2	-0.49	-0.487	-0.53	-1.194	2.427	0.7	0.24	0.47	1
10	133.05354	29.4108	0.086	-22.959	2.63	0.970	2.3	13.98	35.33	2.3	3.4	1.29	0.297	-0.76	-0.781	2.399	0.7	0.38	0.20	1
11	216.32744	40.4898	0.083	-22.035	1.97	0.964	-0.0	10.82	12.82	4.8	4.5	0.48	-0.115	-1.70	-0.038	2.326	0.7	0.47	0.23	1
12	191.71340	0.2970	0.089	-23.248	2.94	1.006	4.0	20.44	14.73	7.5	6.0	-0.56	-0.271	-0.65	1.150	2.505	0.6	0.36	0.17	1
13	134.52059	1.1537	0.071	-22.262	1.94	0.997	2.2	26.81	25.39	9.4	9.0	-0.03	-0.108	-1.19	0.727	2.404	0.8	0.64	0.35	1
14	117.99395	20.7490	0.077	-21.775	1.83	0.954	1.3	7.37	8.38	4.5	4.2	1.14	-0.102	-1.04	-0.145	2.282	0.5	0.53	0.16	1
15	9.36782	15.6263	0.080	-22.800	2.42	0.987	2.0	11.72	10.64	6.4	5.1	-0.06	-0.096	-1.15	0.260	2.371	0.9	0.10	0.11	1
16	133.05970	29.3385	0.085	-22.196	1.89	0.993	2.3	8.64	12.85	6.1	6.5	0.15	-0.046	-1.04	0.646	2.457	0.8	0.74	0.25	1
17	325.61206	-6.5868	0.088	-22.750	2.28	0.979	3.4	26.36	35.56	9.9	10.2	2.42	-0.070	-0.93	-0.050	2.409	0.9	0.19	0.09	1
18	358.77843	-9.3756	0.074	-22.516	2.49	0.981	4.2	4.28	4.92	3.6	3.6	0.66	-0.139	-0.98	0.168	2.387	0.7	0.35	0.41	1
19	188.89591	1.8937	0.078	-22.520	2.16	1.025	3.6	37.61	25.27	8.6	7.0	-0.01	-0.223	-1.04	1.568	2.520	0.7	0.47	0.25	1
20	195.28142	-3.4480	0.083	-22.761	2.74	1.007	5.6	10.16	12.72	4.9	4.7	0.46	-0.086	-1.11	1.070	2.425	0.9	0.57	0.34	1
21	354.57353	15.6689	0.066	-22.600	2.68	0.973	1.7	8.45	14.56	2.7	4.0	2.66	0.044	-1.77	-0.122	2.361	0.8	0.21	0.23	1
22	129.81595	28.8441	0.079	-23.281	3.04	0.993	4.6	4.51	6.14	2.1	2.4	0.20	-0.203	-1.10	0.122	2.543	0.7	0.78	0.38	1
23	230.21770	48.6607	0.074	-23.126	3.15	0.943	4.0	10.66	12.67	4.7	4.8	-0.72	-0.102	-0.40	-3.176	2.529	1.0	0.27	0.45	1
24	228.00073	36.6520	0.066	-22.827	2.91	0.980	0.9	11.04	14.23	3.2	3.3	-1.16	0.059	-0.49	-0.078	2.417	0.7	0.60	0.14	1
25	234.78742	33.6881	0.070	-22.555	1.88	1.016	3.8	20.37	20.19	9.9	10.4	0.09	-0.129	-0.84	1.299	2.458	0.7	0.46	0.45	1
26	172.88388	12.6997	0.081	-22.306	1.85	0.972	1.0	7.00	9.99	2.4	2.6	-0.04	-0.108	-1.23	0.017	2.434	0.4	1.46	0.31	0

Table 2—Continued

ID	R.A.	Dec.	$z$	$^{0.1}M_r$	$\Delta M$	$^{0.1}g-r$	$\delta_N$	$r_{e,g}$	$r_{e,r}$	$n_g$	$n_r$	$a_4(\times 100)$	$\nabla(g-r)$	$\log L_X$	$\delta_{CM}$	$\log \sigma_0$	$\log Age$	$[Z/H]$	$[\alpha/Fe]$	FLAG
(1)	(2)	(3)	(4)	(5)	(6)	(7)	(8)	(9)	(10)	(11)	(12)	(13)	(14)	(15)	(16)	(17)	(18)	(19)	(20)	(21)
27	20.09644	-0.0790	0.077	-23.128	3.01	1.003	1.6	32.20	39.10	4.8	5.0	-0.42	-0.133	-1.00	1.110	2.543	0.8	0.40	0.32	0
28	180.40768	1.1980	0.082	-22.225	2.14	0.903	-2.6	10.41	9.42	4.7	9.2	2.29	-0.848	-0.85	-1.773	2.197	0.6	0.09	0.03	0
29	118.18416	45.9493	0.052	-22.167	2.05	0.963	2.3	6.06	5.78	4.5	4.8	-0.45	-0.042	-0.96	-0.144	2.336	0.7	0.23	0.17	0
30	168.84945	54.4441	0.070	-22.802	1.99	0.939	2.6	7.22	7.38	6.3	5.6	-0.89	-0.041	-1.42	-1.795	2.349	1.0	0.09	0.25	2
31	232.31104	52.8640	0.073	-22.927	2.17	0.995	3.2	21.23	24.43	9.8	8.6	-0.34	0.017	-0.36	0.602	2.454	0.8	0.60	0.41	2
32	122.59694	42.2739	0.064	-22.719	2.40	1.013	3.7	4.56	5.02	2.4	2.9	0.10	-0.321	-1.31	1.298	2.571	0.9	0.63	0.21	2
33	184.62019	42.4610	0.073	-22.029	1.93	0.925	-0.4	9.19	9.73	5.1	4.6	-0.05	-0.054	-1.23	-1.015	2.284	0.9	0.15	0.17	2
34	254.08789	39.2752	0.062	-22.595	2.42	0.976	3.2	294.65	50.08	10.7	10.1	-1.20	-0.700	-1.01	-0.038	2.422	0.6	0.48	0.31	2
35	129.46447	26.5988	0.088	-22.705	1.88	0.903	2.2	6.32	8.82	6.2	6.3	-0.39	-0.069	-0.99	-2.875	2.413	0.5	0.92	0.09	2
36	134.49123	30.3439	0.086	-22.817	2.26	0.949	1.2	15.11	14.76	7.4	6.5	-0.10	-0.147	-0.57	-1.422	2.439	0.9	0.11	0.41	2
37	133.51888	29.0535	0.084	-22.938	2.50	1.002	4.6	8.06	13.29	2.9	3.6	1.72	-0.099	-0.49	0.964	2.463	0.9	0.35	0.36	2
38	237.97868	27.8640	0.082	-21.860	1.81	0.979	2.8	8.80	13.18	2.9	4.1	-0.01	-0.327	0.29	0.421	1.996	0.7	0.56	0.29	2
39	136.68638	3.6002	0.072	-22.123	1.90	0.893	-1.5	12.94	21.63	10.9	10.2	0.97	0.146	-0.51	-1.928	2.209	0.5	-0.07	0.05	2
40	144.40096	7.9180	0.093	-21.778	1.75	0.925	-1.3	2.70	4.25	4.2	4.4	0.91	-0.050	-1.40	-0.824	2.270	0.5	0.20	0.45	2
41	141.65320	3.4606	0.088	-22.235	2.15	0.954	3.3	4.45	7.72	4.8	5.9	-0.06	-0.075	-1.24	-0.427	2.422	0.9	0.21	0.19	2
42	178.15655	3.4727	0.081	-22.771	2.22	0.964	3.0	5.71	9.31	1.6	2.9	0.41	-0.625	0.03	-0.665	2.417	0.8	0.54	0.50	2
43	7.36845	-0.2126	0.060	-22.322	1.85	0.981	5.3	4.82	4.83	2.7	2.5	0.47	0.019	-1.35	0.288	2.390	0.8	0.41	0.32	2
44	216.19754	2.6644	0.053	-22.400	1.95	0.961	3.4	7.04	6.69	4.5	4.5	1.04	-0.009	-0.90	-0.344	2.401	0.8	0.34	0.25	2
45	223.93717	-0.3062	0.083	-22.295	1.92	0.905	1.7	1.09	1.49	2.0	2.4	0.91	-0.369	-0.81	-1.818	2.440	0.8	0.24	0.20	2
46	350.73485	-10.0456	0.084	-22.368	2.24	0.989	5.6	4.94	10.10	5.6	7.8	1.13	0.015	-1.10	0.477	2.444	0.9	0.32	0.36	2